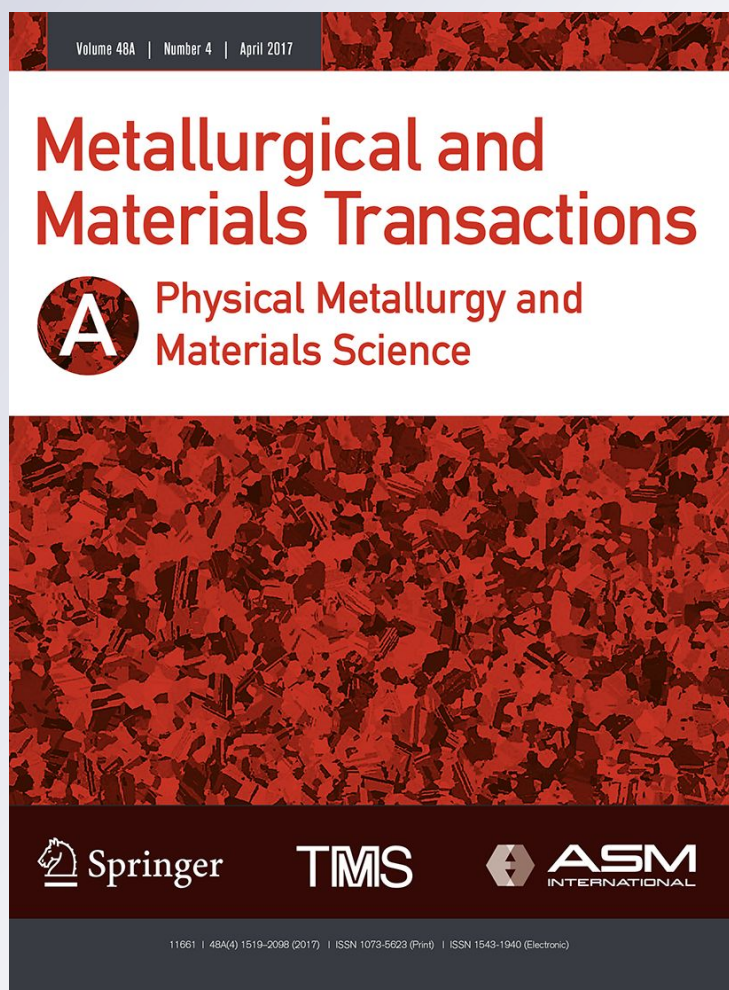# A Pore-Centric Model for Combined Shrinkage and Gas Porosity in Alloy Solidification

Vahid Khalajzadeh, Kent D. Carlson, Daniel G. Backman & Christoph Beckermann

Springer

Springer

A Pore-Centric Model for Combined Shrinkage and Gas Porosity in Alloy Solidification

VAHID KHALAJZADEH, KENT D. CARLSON, DANIEL G. BACKMAN, and CHRISTOPH BECKERMANN

A unified model has been developed for combined gas- and shrinkage-induced pore formation during solidification of metal alloys. The model is based on a pore-centric approach, in which the temporal evolution of the pore radius is calculated as a function of cooling rate, thermal gradient, gas diffusion, and shrinkage. It accounts for the effect of porosity formation on the liquid velocity within the mushy zone. Simulations for an aluminum alloy show that the porosity transitions smoothly from shrinkage-induced to gas-induced as the Niyama value is increased. A Blake (cavitation) instability is observed to occur when the porosity is both gas- and shrinkage-driven. A revised dimensionless Niyama curve for pure shrinkage is presented. The experimentally observed gas porosity trend that the pore volume decreases with increasing cooling rate is well predicted. The pore-centric formulation allows the present model to be solved locally, at any point in a casting, during a regular casting simulation.

I. INTRODUCTION

PREMIUM-QUALITY superalloy, titanium, ferrous, and aluminum casting suppliers for the aerospace and automotive sectors are competitively driven to produce higher quality and lower cost components, with shorter process development time. Both casting shrinkage porosity and gas porosity have long posed quality issues that can impair cast component performance associated with reduced fatigue life, reduced tensile and creep capability, and the potential occurrence of leakage-pathways for pressurized parts. Casting solidification software developers have been working with foundries to establish and implement porosity modeling modules that capture the fundamental physics of porosity formation, while respecting and adhering to the computational constraints imposed by the size and complexity of modern castings. Once verified and validated, these porosity models provide an opportunity to help guide casting development and to enable optimization of process parameters and gating/riser design, while also reducing the requisite number of empirically based casting development trials.

The differences between the two types of porosity mentioned above (shrinkage porosity and gas porosity) are illustrated in Figure 1, which contains photographs of metallographic sections containing each type of porosity. Shrinkage porosity (Figure 1(a)) is caused by the density change from liquid to solid during solidification; it forms when the accompanying shrinkage can no longer be fed by flow of the liquid. It often forms late in solidification, when the solid dendritic network has a low permeability and is rigid. As a result, the porosity takes on the tortuous shape of the remaining spaces between the dendrites. Gas porosity (Figure 1(b)), on the other hand, occurs when the melt contains relatively large amounts of a dissolved gas. In this instance, pores can form much earlier in solidification, and therefore, the pores have the freedom to adopt a more spherical shape. The physics underlying the formation of both types of porosity are related, as explained in the next section, and there are certainly instances in metal casting where both mechanisms, shrinkage and gas, play a role simultaneously.

Casting porosity has been the subject of numerous solidification research studies since the 1960s. Piwonka and Flemings[1] and Kubo and Pehlke[2] identified porosity formation mechanisms and mathematical models to describe porosity evolution. Over the next four decades, advances in the understanding and modeling of porosity formation were made by a number of solidification researchers.[3–10] These advances included the following: refining the description of the liquid pressure drop associated with flow in the mushy zone; new or improved thermodynamic approximations; modeling the diffusive transport of liquid phase gas-solute toward growing gas pores; including the influence of the dispersion pore-nuclei potency upon final pore size distributions; and *in situ* pore measurement during solidification. Much of this work has been summarized in review papers.[11,12]

The combined shrinkage- and gas-induced porosity model presented in this paper has been influenced by these earlier developments, but the trajectory and detail of the present research most strongly follow papers by

VAHID KHALAJZADEH, KENT D. CARLSON, and CHRISTOPH BECKERMANN are with the Department of Mechanical and Industrial Engineering, University of Iowa, Iowa City, IA 52242. Contact e-mail: becker@engineering.uiowa.edu DANIEL G. BACKMAN is with the Backman Materials Consulting, LLC, Saugus, MA 01906.
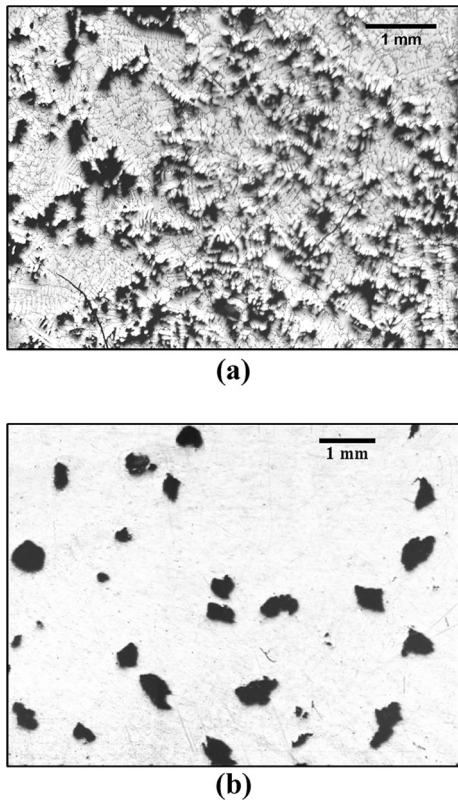
(a)

(b)

Fig. 1—Typical porosity defects on metallographic sections of aluminum alloy castings: (*a*) shrinkage porosity; (*b*) gas porosity.

Carlson and Beckermann that address shrinkage porosity[13] and combined shrinkage and gas porosity.[14] These studies are briefly discussed in the following paragraphs.

For decades, foundry process engineers have qualitatively predicted the presence and severity of casting shrinkage porosity using the empirically derived Niyama criterion,[15] $Ny = G / \sqrt{\dot{T}}$, where G is the thermal gradient, and $\dot{T}$ is the cooling rate. While useful, this criterion has shortcomings. First of all, since the Niyama criterion does not utilize material properties or solidification path information, the critical Ny value that is used to detect the onset of shrinkage porosity is dependent on the casting alloy and process, and must be empirically determined. Second, the Niyama criterion cannot be used to quantitatively determine the amount of porosity that will form. Carlson and Beckermann[13] proposed a novel procedure for the prediction of shrinkage porosity by developing a dimensionless form of the Niyama criterion ($Ny*$) that incorporates mushy zone physics and alloy properties. This research showed that $Ny*$ calculations performed during computer casting simulations can be used to directly predict shrinkage pore volume fractions throughout the casting, with knowledge of the alloy's solid fraction-temperature curve and total solidification shrinkage. Note that, this criterion model cannot be used to predict gas porosity. An experimental validation of the $Ny*$ model has recently been reported by Guo et al. for Ni-based superalloy castings.[16]

Carlson et al.[14] developed a volume-averaged model that predicts both gas-related and shrinkage-related porosity by accounting for the simultaneous effects of pressure drop and hydrogen diffusion on pore growth. In this model, the gas species conservation equation was coupled with equations for feeding flow and the pressure field in solidifying metal. Yao et al.[17] applied this model in a pore formation investigation of A356 aluminum alloy and showed that the model developed by Carlson et al.[14] provided acceptable accuracy for gas porosity predictions in aluminum alloys. The volume-averaged model of Reference 14 requires the coupled solution of transient conservation equations over the entire casting domain. While such generality may be needed for predicting porosity for complex casting geometries and solidification conditions, the model is computationally intensive and therefore difficult to apply for typical commercial casting simulations. Indeed, this model does not provide straightforward evaluation of the porosity volume fraction at any point in a casting as a function of the local cooling conditions, gas content and alloy properties, in contrast to the $Ny*$ model of Reference 13 for pure shrinkage.

The present study develops a unified gas- and shrinkage-related porosity model that relies on the solution of local point equations. It extends and generalizes the $Ny*$ shrinkage model of Reference 13 to include the effect of a dissolved gas. The model is simple enough that it can be used as part of a standard casting simulation to predict the extent of the porosity at any point in the casting. The following section describes the model development. Subsequently, the model is applied in parametric studies designed to investigate the effects of model parameters on porosity formation. The parametric studies are performed for an aluminum alloy commonly used in castings. Finally, a comparison between model predictions and experimental data, available within the literature, provides initial model validation.

II. MODEL DESCRIPTION

The porosity model developed herein relies heavily on the prior work of References 13 and 14, adopting many of the concepts and relationships established in these earlier studies. However, the present work differs in a significant way by adopting a pore-centric model framework that accounts for both gas- and shrinkage-induced porosity. As with earlier work, this model focuses on the growth of pores that heterogeneously nucleate on entrained oxide films or other inclusions[14] when appropriate thermodynamic conditions are satisfied within the mushy zone. The following subsections present the overarching porosity growth equation, the criterion for pore nucleation, and ancillary equations that describe the liquid pressure variation and solute transport, which are needed to solve the growth equation. The final subsection summarizes the model's overall system of equations and solution procedure.

A. *The Porosity Growth Equation*

The present model uses the ideal gas law and the Young–Laplace equation to formulate a unified porosity model that relates pore radius change to changes in liquid pressure, local temperature, and pore gas content. Consider an isolated spherical gas pore of radius r_p surrounded by molten metal alloy at local melt pressure, P_l; the local temperature is T (absolute); and the interface separating the pore and molten alloy is characterized by surface tension, σ. Based on the Young–Laplace equation, the gas pressure inside the pore, P_p, can be described by

$$P_p = P_l + P_\sigma \quad [1]$$

where P_σ is the capillary pressure due to surface tension, defined by $P_\sigma = 2\sigma/r_p$. Assuming that gas within the pore is adequately described by the ideal gas law, the pore pressure is described by

$$P_p = \frac{m_p \Re T}{V_p} \quad [2]$$

where m_p is the mass of the pore; $\Re$ is the gas constant for the gas species; and V_p is the volume of a spherical pore ($V_p = 4\pi r_p^3/3$). Note that, the assumption that pores are spherical in shape is no longer valid after pores grow sufficiently large such that the pore shape is constrained by the morphology of the enveloping dendritic network. However, the model includes an impingement factor that attempts to correct the error in this assumption associated with contact between pore and solid; this will be addressed in Section II–D. By combining Eqs. [1] and [2], the pore can be described by the following equation, which contains four variables: r_p, P_l, m_p, and T.

$$P_l r_p^3 + 2\sigma r_p^2 = \frac{3 m_p \Re T}{4\pi} \quad [3]$$

The corresponding pore growth differential equation is obtained by applying the time-derivative operator to Eq. [3] and rearranging terms:

$$\frac{\partial r_p}{\partial t} = \frac{1}{3 P_l r_p^2 + 4\sigma r_p}\left[\frac{3\Re T}{4\pi}\frac{\partial m_p}{\partial t} + \frac{3\Re m_p}{4\pi}\frac{\partial T}{\partial t} - r_p^3 \frac{\partial P_l}{\partial t}\right] \quad [4]$$

In Eq. [4], the pore growth rate ($\partial r_p/\partial t$) depends on the three time-derivative terms within the brackets: the rates of change of pore mass ($\partial m_p/\partial t$), temperature ($\partial T/\partial t$), and liquid pressure ($\partial P_l/\partial t$). In order to have a closed set of equations, each of these three terms must be defined explicitly. In the present study, the cooling rate, denoted by $\dot{T}$, is assumed constant and set to a specified value, such that $\partial T/\partial t = -\dot{T}$. Expressions for the two remaining partial differentials with respect to time are developed in Sections II–B and II–C, respectively. Note that due to the denominator in front of the square brackets, Eq. [4] exhibits a potential singularity when $P_l = -4\sigma/3r_p$; this is the so-called Blake

threshold.[18] This singularity induces unbounded pore growth or collapse. The physics of bubble dynamics during cavitation are not included in the present model.[19] However, the singularity was found to occur for some combinations of model input parameters, as discussed later in Section III–B–3.

The pore radius growth modeled by Eq. [4] is applicable to purely shrinkage-induced, purely gas-induced, and mixed-mode porosity. A literature review of pore-centric porosity models has identified that the model of Stefanescu and Catalina[20] shares some common elements with Eq. [4] above. However, their pore growth equation (Eq. [24] in Reference 20) is limited to gas porosity, and its derivation is flawed by a failure to account for the mutual dependence of pore volume and capillary pressure upon pore radius during differentiation.

B. *Pore Nucleation*

The heterogeneous nucleation of a pore at pressure P_p within a solidifying mushy zone requires sufficient energy to overcome the surface energy of the pore (*i.e.*, the surface tension at the interface between the pore and the liquid metal). For the analysis of pore nucleation, the mean radius of an emergent pore is denoted by $r_{p,0}$, which is associated with a nucleation capillary pressure: $P_{\sigma,\text{nuc}} = 2\sigma/r_{p,0}$. Therefore, the necessary condition for pore nucleation is expressed by the following inequality:

$$P_p - P_l \geq P_{\sigma,\text{nuc}} \quad [5]$$

Although nucleation and growth of a pore within the mushy zone are not equilibrium processes, it is generally acknowledged that local equilibrium exists at both liquid-solid and liquid-gas interfaces, relative to solute exchange between adjacent phases. For liquid-gas interfaces, this equilibrium is often described using Sievert's law:

$$P_p = P_{\text{atm}}\left(\frac{C_{lp}f}{K_e}\right)^2 \quad [6]$$

where P_{atm} is atmospheric pressure, C_{lp} is the equilibrium gas-solute concentration in the liquid at the pore-liquid interface, $K_e = 10^{-\left(\frac{a_1}{T}+b_1\right)}$ (wt pct) is the equilibrium coefficient, which contains constants a_1 and b_1, and f is the activity coefficient for the gas species. Combining Eqs. [5] and [6] yields the following form of the pore nucleation condition:

$$\left[P_{\text{atm}}\left(\frac{C_{lp}f}{K_e}\right)^2 - P_l\right] \geq \frac{2\sigma}{r_{p,0}} \quad [7]$$

This equation shows that in the general case, for a fixed nucleation pore radius, $r_{p,0}$, pore nucleation is promoted by increasing the melt solute concentration at the liquid-nuclei interface and/or by decreasing the surrounding liquid pressure. In the case of pure

shrinkage porosity (*i.e.*, exceedingly low melt gas-solute concentration), C_{lp} approaches zero and pore nucleation depends solely on the nucleation radius and the pressure of the surrounding liquid. Note that before nucleation, C_{lp} is assumed to be equal to the average gas concentration in the melt (*i.e.*, $C_{lp} = C_l$), where the average melt gas concentration, C_l, is obtained from the overall gas species mass balance, which will be discussed in Section II–D.

C. *Liquid Pressure Variation*

A schematic diagram of a mushy zone, Figure 2, shows the general context of the model along with key nomenclature. The solid is depicted as equiaxed dendritic grains because the model is later applied to an aluminum alloy, but the type of grain structure does not play a role in the model equations. The spatial coordinate, x, is measured from the beginning of the mushy zone. The distance L is the mushy zone length, while G is the temperature gradient and R is the isotherm velocity. The location denoted x_{cr} represents the critical location at which pores form, and l is the location at which the liquid volume is reduced to zero (because the local volume is entirely filled with solid and porosity). Within the mushy zone, the temperature gradient, $(G = -dT/dx)$, and cooling rate, $(\dot{T} = -dT/dt)$, are each assumed constant, yielding a constant isotherm velocity, R, given by $R = \dot{T}/G$. The linearity and relationships among these thermal and growth rate metrics provide a simple means to translate between spatial and time derivatives, that is, $d/dt = R(d/dx)$. This relationship will be used later in this section.

The porosity model uses a representative volume for flow that is composed of some combination of liquid metal (*l*), solid metal (*s*), and porosity (*p*), such that the volume fractions satisfy the expression $g_l + g_s + g_p = 1$. By assuming that pores and solid metal are stationary, the 1-D mixture continuity equation can be written as

$$\frac{\partial}{\partial t}\left(g_s\rho_s + g_l\rho_l + g_p\rho_p\right) + \frac{\partial}{\partial x}\left(g_l\rho_l u_l\right) = 0 \qquad [8]$$

where u_l is the liquid velocity in the mushy zone. Assuming the density of liquid metal (ρ_l) and solid metal (ρ_s) are constant, and recognizing that both are much greater than the pore density (*i.e.*, $\rho_s, \rho_l >> \rho_p$), Eq. [8] is approximated by

$$\frac{\partial}{\partial x}\left(g_l u_l\right) = \beta\frac{\partial g_l}{\partial t} + (1+\beta)\frac{\partial g_p}{\partial t}, \qquad [9]$$

where $\beta = (\rho_s - \rho_l)/\rho_l$ is the solidification shrinkage, and $g_l u_l$ is termed the superficial velocity. By invoking the derivative translation relationship developed at the beginning of this section, $d/dt = R(d/dx)$, Eq. [9] is simplified to the following form:

$$d(g_l u_l) = R(\beta dg_l + (1+\beta)dg_p). \qquad [10]$$

In the absence of porosity within the mushy zone, solidification is complete when the local temperature reaches the solidus temperature (at the end of the mushy zone, $x = L$ in Figure 2). However, when porosity forms in the mushy zone, the liquid fraction drops to zero somewhere before the end of the mushy zone (at $x = l$ in Figure 2), where the sum of the solid fraction and the pore fraction becomes unity (and therefore $g_l = 0$ in order to satisfy $g_l + g_s + g_p = 1$). At $x = l$, the pore fraction is $g_p(l)$ and the solid fraction is given by $g_s(l) = 1 - g_p(l)$. Moreover, at the end of solidification, the superficial velocity is equal to zero $(g_l u_l(l) = 0)$.

Using this information, Eq. [10] is integrated from an arbitrary position in the mushy zone to $x = l$ as:

$$\int\limits_{g_l u_l}^{0} d(g_l u_l) = \beta R \int\limits_{g_l}^{0} dg_l + R(1+\beta) \int\limits_{g_p}^{g_p(l)} dg_p. \qquad [11]$$

Integration of this expression yields the following result:

$$g_l u_l = R\left[\beta g_l - (1+\beta)\left(g_p(l) - g_p\right)\right]. \qquad [12]$$

In Eq. [12], the superficial velocity is given as a function of liquid fraction and pore fraction. By replacing the liquid fraction with $g_l = 1 - g_s - g_p$, the superficial velocity can be expressed as a function of solid fraction and pore fraction, which is more convenient:

$$g_l u_l = R\left[\beta\left(1 - g_p(l) - g_s\right) - \left(g_p(l) - g_p\right)\right]. \qquad [13]$$

In the absence of porosity ($g_p = 0$), the above equation reduces to the well-known result for the shrinkage velocity in a mushy zone: $u_l = R\beta$.[13] Examination of the two terms on the right-hand side (RHS) of Eq. [13] reveals the physics that govern the superficial velocity in the presence of porosity. The first term results in shrinkage-induced liquid flow toward the solidus isotherm (*i.e.*, positive x-direction in Figure 2), and the second term results in liquid flow toward the liquidus isotherm (*i.e.*, negative x-direction), resulting from pore growth. The balance of these two terms defines the local direction and magnitude of superficial velocity within the mushy zone. The final pore fraction, $g_p(l)$, in Eq. [13] is not known *a priori*, but rather must be determined as part of the numerical solution procedure (see Section II–E).

The liquid momentum equation is given by Darcy's law as

$$g_l u_l = -\frac{K}{\mu_l}\frac{\partial P_l}{\partial x}, \qquad [14]$$

where P_l is the local liquid pressure and μ_l is the liquid dynamic viscosity. The permeability in the mushy zone (K) is assumed to be given by

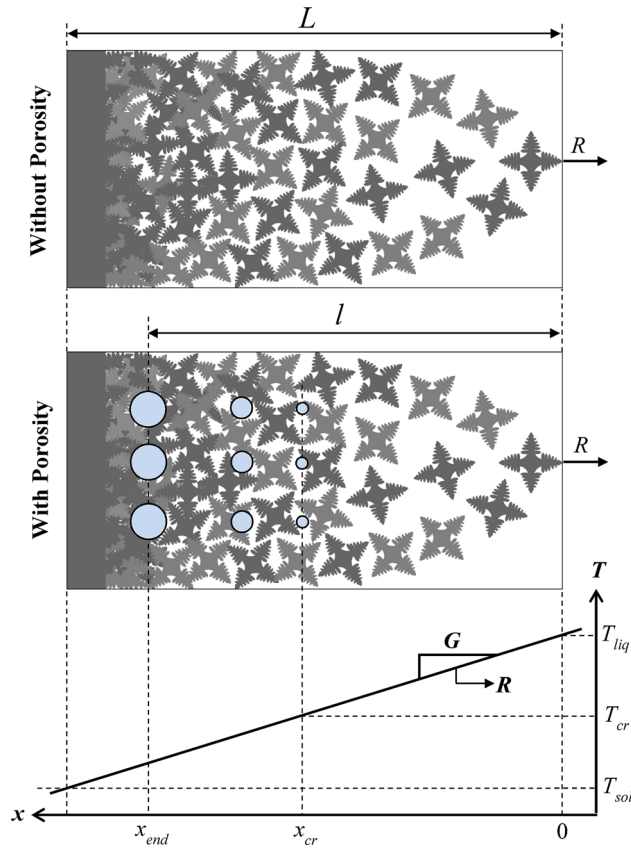$$K = \frac{\lambda_2^2}{180}\frac{(1 - g_s)^3}{g_s^2}, \qquad [15]$$

Fig. 2—Schematic of a mushy zone, with and without porosity, solidifying with a constant isotherm velocity, R, and temperature gradient, G (Color figure online).

Fig. 3—Schematic showing the variation of the gas species concentration in the liquid around a spherical pore (Color figure online).

where λ_2 is the secondary dendrite arm spacing (SDAS), which is expressed as a function of cooling rate: $\lambda_2 = C_\lambda \dot{T}^{-1/3}$. By combining Eqs. [13] through [15], then replacing in Darcy's law the spatial derivative with a corresponding time derivative, and finally rearranging terms, the time rate of change of the liquid pressure is given by

$$\frac{\partial P_l}{\partial t} = -\frac{\mu_l}{K} R^2 \left[\beta \left(1 - g_p(l) - g_s \right) - \left(g_p(l) - g_p \right) \right]. \quad [16]$$

The initial condition for this equation is that at $t = 0$, the liquid pressure is equal to the pressure at the liquidus isotherm, which is taken to be equal to the atmospheric pressure, P_{atm}, in the present study. In Eq. [16], as long as the difference between the shrinkage-related term (first term in the bracket) and the porosity-related term (second term in the bracket) is positive, the time rate of change of the liquid pressure is negative. When the balance reverses, the change in liquid pressure becomes positive. Obviously, the liquid pressure remains constant when the two terms are of equal magnitude.

As mentioned in the Introduction, the Niyama criterion (Ny) is widely used in metal casting industries as a qualitative metric to gauge the level of casting shrinkage porosity. This criterion involves only local
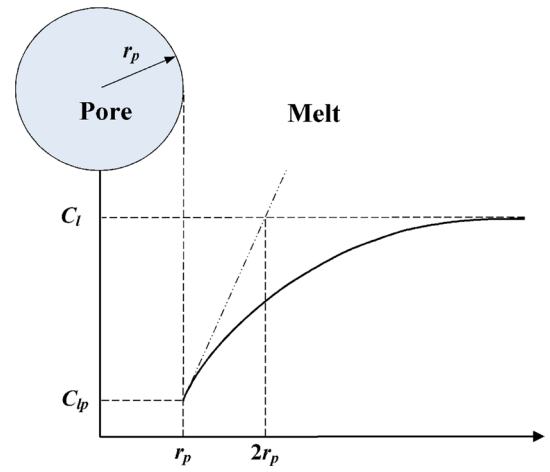
thermal parameters and is defined as the ratio of the thermal gradient to the square root of the cooling rate, $Ny = G / \sqrt{\dot{T}}$. As discussed earlier, the isotherm velocity is the ratio of the cooling rate to the thermal gradient, $R = \dot{T}/G$. By combining these two definitions, the isotherm velocity can be expressed as a function of cooling rate and Niyama criterion by $R = \sqrt{\dot{T}} / Ny$. The introduction of this relationship into Eq. [16] yields an alternative expression for the time rate of change of the liquid pressure:

$$\frac{\partial P_l}{\partial t} = -\frac{\mu_l \dot{T}}{K N y^2} \left[\beta \left(1 - g_p(l) - g_s \right) - \left(g_p(l) - g_p \right) \right]. \quad [17]$$

D. Mass Diffusion Rate

The mass of the gas inside the pores increases as gas solute diffuses through the liquid toward the liquid-pore interfaces and into the pores. As illustrated in Figure 3, this occurs when the equilibrium gas concentration in the liquid at the liquid-pore interface, C_{lp}, is lower than the average gas solute concentration in the liquid, C_l. Based on Fick's 1st law, the mass diffusion rate toward a gas pore can be expressed by

$$\frac{1}{A_p} \frac{\partial m_p}{\partial t} = \rho_l D_l \left. \frac{\partial C_l}{\partial r} \right|_{r=r_p}, \quad [18]$$

where ρ_l is the liquid density, D_l is the gas-solute mass diffusion coefficient in the melt and A_p is the area of the interface between liquid and pores. The interfacial gas-solute concentration gradient (*i.e.*, the last term on the right-hand side of Eq. [18]) can be calculated by applying an analytical solution for a quasi-steady-state diffusion boundary layer surrounding a sphere,[14] as shown in Figure 3. Rearranging terms in Eq. [18], the mass diffusion flux becomes

$$\frac{\partial m_p}{\partial t} = \rho_l D_l A_p \frac{C_l - C_{lp}}{r_p} \qquad [19]$$

In Eq. [19], the gas-solute mass diffusion coefficient is a function of absolute temperature (K), given by $D_l = D_0 \exp\left(\frac{-a_2}{T}\right)$ m^2/s, where D_0 and a_2 are constants. The pore-liquid interface area is approximated as $A_p = 4\pi r_p^2 \varphi$, where φ is an impingement factor, expressed as $\varphi = (1 - g_s)^m$.

The impingement factor accounts for how pore growth is influenced by contact between a growing pore and the surrounding mushy zone dendritic network. For example, as volume fraction solid, g_s, increases during solidification, the pore surface area in contact with solid, A_{ps}, will increase while the pore surface area in contact with mushy-zone liquid, A_{pl}, will decrease. Correspondingly the decreasing ratio, A_{pl}/A_{ps}, will reduce the diffusive transport of gas-solute into the pore (thereby reducing its growth rate) because the diffusion rate of gas-solute is higher in the liquid than in the solid. For example, research by Felberbaum[21] showed that the hydrogen diffusion rate in Al-Cu solid alloy is only 40 pct of the diffusion rate in the liquid within the mushy zone regime. By necessity, the impingement equation, $\varphi = (1 - g_s)^m$, is a phenomenological relationship and the exponent, m, must be determined *via* calibration, because there is no means to apply stereological principles to achieve a unique relationship. This difficulty arises because of the morphological diversity among dendritic structures that depend on alloy, solidification mode (*i.e.*, equiaxed *vs* columnar), and solidification conditions (*e.g.*, G, R, and $\dot{T}$) as they influence dendrite length scales and the degree of coarsening within and along the mushy zone.

Re-arranging Eq. [6], the equilibrium solute concentration at the liquid-pore interface is described by Sievert's law as follows:

$$C_{lp} = \frac{K_e}{f}\left(\frac{P_p}{P_{atm}}\right)^{1/2}, \qquad [20]$$

where the parameters, K_e and f, in this equation are the gas equilibrium coefficient and activity coefficient, respectively.

By neglecting the advection and diffusion of gas solute in the liquid, and assuming that pores are composed of a single gas only (*i.e.*, $C_p = 1$), the overall gas species mass balance can be written as

$$g_s \rho_s \kappa_{sl} C_l + g_l \rho_l C_l + g_p \rho_p = \rho_l C_0, \qquad [21]$$

where κ_{sl} is the gas partition coefficient between solid and liquid metal, which is given by $\kappa_{sl} = C_s/C_l$, and C_0 is the initial gas concentration in melt. Using $g_l + g_s + g_p = 1$ and solving Eq. [21] for C_l yields:

$$C_l = \frac{C_0 - g_p \rho_p / \rho_l}{1 - g_p + g_s((1+\beta)\kappa_{sl} - 1)} \qquad [22]$$

where ρ_p is the density of a pore, calculated from the ideal gas law, $\rho_p = P_p / \Re T$, and g_p is the pore volume fraction, defined by $g_p = n_p 4\pi r_p^3 / 3$, where n_p is the number of pores per unit volume.

E. *Model Assembly and Computational Details*

The computational model is organized using the pore growth relationship, Eq. [4], and the ancillary relationships for the time-derivative terms on the RHS of Eq. [4] that were developed in Sections II–C and II–D. The liquid pressure term is modeled by Eq. [17], the mass diffusion term is modeled by Eq. [19], and the temperature term (cooling rate) is assumed to be constant. When the nucleation condition has not been met, the RHS of Eq. [4] is negative and the pore radius remains constant and equal to the initial (nucleation) value, $r_{p,0}$. The pore radius begins to increase when the nucleation condition is met and the RHS of Eq. [4] becomes positive. Sievert's law, Eq. [20], is used in different ways before and after pore nucleation. Before porosity forms, the model assumes that the equilibrium solute concentration at the pore-liquid interface, C_{lp}, is equal to the gas solute concentration in the liquid (*i.e.*, $C_{lp} = C_l$), and Sievert's law is used to calculate the pore pressure, P_P. Once porosity forms, the pore pressure is determined by the Young–Laplace equation (Eq. 1), and Sievert's law is used to calculate C_{lp}. All essential modeling equations are listed for convenience in Table I. Given that the system of equations is nonlinear, particularly when the RHS multiplicand of Eq. [4] approaches the Blake singularity, a hybrid implicit-explicit numerical scheme has been applied, using a very fine time step on the order of 10^{-6} seconds.

The numerical solution of the overarching Eq. [4] acknowledges that the final pore fraction in Eq. [17], $g_p(l)$, is not known *a priori*, but instead must be determined using an iterative prediction-correction algorithm. In formulating this sub-algorithm, the logic applied is that when the correct value of $g_p(l)$ is found, the pore radius increases immediately after nucleation; if this condition is not met (*i.e.*, when the RHS of Eq. [4] is negative), the computed $g_p(l)$ is incorrect and iterative search then continues until an acceptable $g_p(l)$ value is identified, as confirmed by subsequent successful convergence.

The computations performed for this study employ an A356 aluminum alloy with the composition listed in Table II. The gas solute is assumed to be hydrogen, the dominant gas solute for aluminum alloys. This choice is not intended to imply that the model is only valid for aluminum alloys; the model could be applied to any metal alloy-gas combination. The solid fraction curve of the A356 alloy was determined using JMatPro™ software;[22] the resulting solid fraction curve is shown in Figure 4. Calculated liquidus and solidus temperatures are T_{liq} = 889 K (616 °C) and T_{sol} = 824 K (551 °C), respectively. The solid fraction curve in Figure 4 contains two very noticeable slope discontinuities. The first discontinuity encountered upon cooling occurs at 847 K (574 °C). This large, sharp discontinuity in the solid fraction slope corresponds to the initial formation of the primary eutectic (Si) phase. The second, smaller slope discontinuity at 830 K (557 °C) is associated with the formation of the phase Mg$_2$Si. Further details concerning

Table I. Summary of the Equations Used in the Porosity Model

Name of the Equation	Mathematical Formula
Pore Growth Rate	$\dfrac{\partial r_p}{\partial t} = \dfrac{1}{3P_l r_p^2 + 4\sigma r_p}\left[\dfrac{3\Re T}{4\pi}\dfrac{\partial m_p}{\partial t} + \dfrac{3\Re m_p}{4\pi}\dfrac{\partial T}{\partial t} - r_p^3\dfrac{\partial P_l}{\partial t}\right]$
Liquid Pressure Drop	$\dfrac{\partial P_l}{\partial t} = -\dfrac{\mu_l \dot{T}}{KNy^2}\left[\beta\left(1 - g_p(l) - g_s\right) - \left(g_p(l) - g_p\right)\right]$
Mass Diffusion Rate	$\dfrac{\partial m_p}{\partial t} = \rho_l D_l A_p \dfrac{C_l - C_{lp}}{r_p}$
Cooling Rate	$\dfrac{\partial T}{\partial t} = -\dot{T}$
Gas Concentration in Liquid	$C_l = \dfrac{C_0 - g_p \rho_p / \rho_l}{1 - g_p + g_s((1+\beta)\kappa_{sl} - 1)}$
Equilibrium Concentration (Sievert's law)	$C_{lp} = \dfrac{K_e}{f}\left(\dfrac{P_p}{P_{atm}}\right)^{1/2}$
Pore-Liquid Interface Area	$A_p = 4\pi r_p^2 (1 - g_s)^m$
Equilibrium Coefficient	$\log_{10} K_e = -\left(\dfrac{a_1}{T} + b_1\right)$
Mass Diffusion Coefficient	$D_l = D_0 \exp\left(\dfrac{-a_2}{T}\right)$
Pore Fraction	$g_p = n_p \dfrac{4}{3}\pi r_p^3$
Ideal Gas Law	$\rho_p = \dfrac{P_p}{\Re T}$
Young–Laplace	$P_p = P_l + \dfrac{2\sigma}{r_p}$
Niyama Criterion	$Ny = \dfrac{G}{\sqrt{\dot{T}}}$
Linear Temperature Profile	$T = T_{liq} - \dot{T}t$
Kozeny–Carman	$K = \dfrac{\lambda_2^2}{180}\dfrac{(1 - g_s)^3}{g_s^2}$
Secondary Dendrite Arm Spacing (SDAS)	$\lambda_2 = C_\lambda \dot{T}^{-1/3}$

Table II. Composition of the A356 Aluminum Alloy

Element	Amount (Wt Pct)
Si	7.0
Mg	0.37
Fe	0.10
Ti	0.08
Zn	0.01
Cu	0.01
Mn	0.01
Al	balance

the different phases and their influence upon solidification are discussed in Reference 14. All relevant material properties and parameters used during the simulations performed for this study are listed in Table III.

III. RESULTS AND DISCUSSION

The present pore-centric porosity model has been systematically exercised to study how it responds to melt and solidification parameters, as well as to internal physical model parameters. First, the model is applied to pure shrinkage porosity and to combined shrinkage and gas porosity. The evolution of porosity content and
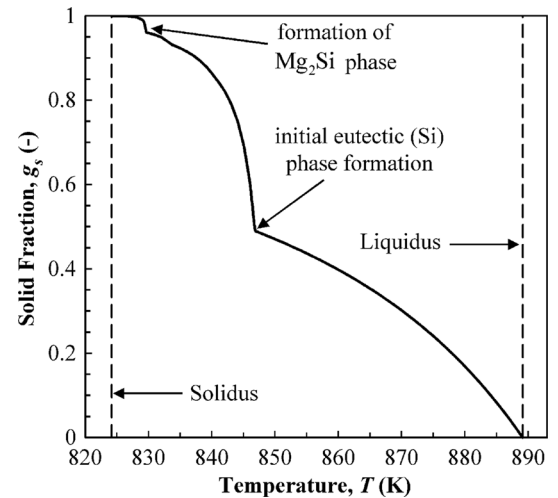

Fig. 4—Solid fraction of A356 aluminum alloy as a function of temperature.

influential internal variables are investigated in detail and parametric sensitivity studies are conducted that focus on the influence of uncertain model constants, Niyama value, cooling rate, and melt gas content upon final porosity percentage. The differences between the present model and

Table III. Material Properties and Parameters Used in the Simulations

Parameter (Units)	Value
Hydrogen Gas Constant, $\Re$ (J/kg K)	4124
Surface Tension, σ (N/m)	0.8
Liquidus Temperature, T_{liq}	889 K (616 °C)
Solidus Temperature, T_{sol}	824 K (551 °C)
Hydrogen Partition Coefficient, $\kappa_{sl}(-)$	0.07
Activity Coefficient, $f(-)$	1.25
Liquid Dynamic Viscosity at Liquidus Temperature, μ_l(Pa.s)	0.00158
Liquid Density at Liquidus Temperature, ρ_l (kg/m^3)	2429.4
Solid Density at Solidus Temperature, ρ_s (kg/m^3)	2572
Solidification Shrinkage, β $(-)$	5.87 pct
Constants in Equilibrium Coefficient Equation for Hydrogen, a_1 and b_1	2691.96 and 1.32
Constants in Diffusion Coefficient Equation for Hydrogen, D_0 and a_2	3.8×10^{-6} and 2315
Constant in Secondary Dendrite Arm Spacing (SDAS) Equation, C_λ	4.09×10^{-5}

the earlier $Ny*$ model[13] for pure shrinkage are investigated in detail. The Blake singularity is discussed further as well. In the final subsection, a calibration of the model for pure gas porosity is presented.

A. *Pure Shrinkage Porosity*

1. *Initial shrinkage porosity simulation*

The current porosity model was first applied to simulate the evolution of porosity under conditions wherein porosity forms solely *via* pure shrinkage, with no gas-solute influence (*i.e.*, $C_0 = 0$). For this case, the pore pressure and the pore gas content are negligibly small. In reality, a pure shrinkage pore will contain vapors of the various alloying elements present. For most industrially relevant casting alloys, including the present aluminum alloy, the alloying element vapor pressures are relatively small and can be neglected. Consequently, all terms in Eq. [4] containing m_p vanish, thereby reducing the equation to the following:

$$\frac{\partial r_p}{\partial t} = \frac{r_p^2}{3P_l r_p + 4\sigma}\left[-\frac{\partial P_l}{\partial t}\right]. \qquad [23]$$

The above simplified equation clearly illustrates the close relationship between pore radius and liquid pressure in the case of pure shrinkage; however, for the sake of generality, this simplified form was not used in the simulations. An initial simulation for the limiting case of $C_0 = 0$, using the full relations and properties in Tables I and III, was performed for a cooling rate of $\dot{T} = 1$ K/s, Niyama value of $Ny = 0.05$ (K-s)$^{0.5}$/mm, nucleation pore radius of $r_{p,0} = 10\,\mu$m, and pore number density of $n_p = 10^{11}$ m^{-3}. The small Ny value for this first simulation was selected to induce significant shrinkage porosity. For the value of nucleation pore radius selected, the nucleation capillary pressure is $P_{\sigma,nuc} = 1.58$ atm (1.6 bar).

The simulation results are shown in Figure 5, which contains plots of the following: (a) liquid pressure, P_l; (b) superficial velocity, $g_l u_l$; and (c) pore volume fraction, g_p. All variables in Figure 5 are plotted against dimensionless time, which is defined as the ratio of simulation time, t, to the local solidification time, t_f, *i.e.*, (t/t_f). Each plot in Figure 5 also contains a curve displaying the solid fraction,

g_s, *vs* dimensionless time. Figure 5(a) shows that, prior to pore nucleation, the liquid pressure decreases in accordance with Darcy's Law, Eq. [14]. The rate of pressure drop increases significantly at the start of primary eutectic phase formation, which occurs at $t/t_f = 0.65$. This is seen as a sharp decrease in the slope of the liquid pressure curve, which is a direct result of the sharp increase in the slope of the solid fraction curve. The liquid pressure continues to drop until it reaches the negative of the nucleation pressure, -1.58 atm. At this point, the equality of the expression given in Eq. [5] is met, *i.e.*, $P_l = -P_{\sigma,nuc}$ (since $P_p = 0$), and porosity nucleates. Following nucleation, pore growth and attendant increasing pore radius reduces the magnitude of the capillary pressure, $P_\sigma = 2\sigma/r_p$, thus causing the liquid pressure to rise because $P_l = -P_\sigma$, as required by the Young–Laplace equation.

The liquid superficial velocity is plotted in Figure 5(b), non-dimensionalized by the isotherm velocity. The variation in the superficial velocity is driven by the local mushy zone liquid pressure gradient. Before nucleation, $g_l u_l$ is positive, and so interdendritic liquid flows toward the fully solidified region (see Figure 2), thereby compensating for solidification shrinkage. However, following nucleation, the superficial velocity becomes negative and then gradually returns back toward zero. The sign of $g_l u_l$ remains negative until solidification is complete, and its magnitude is quite small because pore growth accommodates almost all of the remaining solidification shrinkage. Finally, the evolution of the pore volume is shown in Figure 5(c). The pore volume percentage increases monotonically from the inception of nucleation until all the liquid in the mushy zone has been depleted (*i.e.*, $g_l = 0$), at $t/t_f = 0.93$. Note that the pore volume curve in Figure 5(c) has a significant, sharp increase in slope that occurs at the start of secondary phase (Mg$_2$Si) formation near the end of solidification (at $t/t_f = 0.92$). This slope increase is caused by the corresponding slope increase in the liquid pressure curve at the same time (see Figure 5a), which results from the change in slope of the solid fraction curve when Mg$_2$Si begins to form. Although this occurs shortly before solidification is complete, the pore volume curve becomes so steep that it significantly increases the pore volume, from 0.43 pct at $t/t_f = 0.92$ to the final pore volume of $g_p(l) = 0.62$ pct.
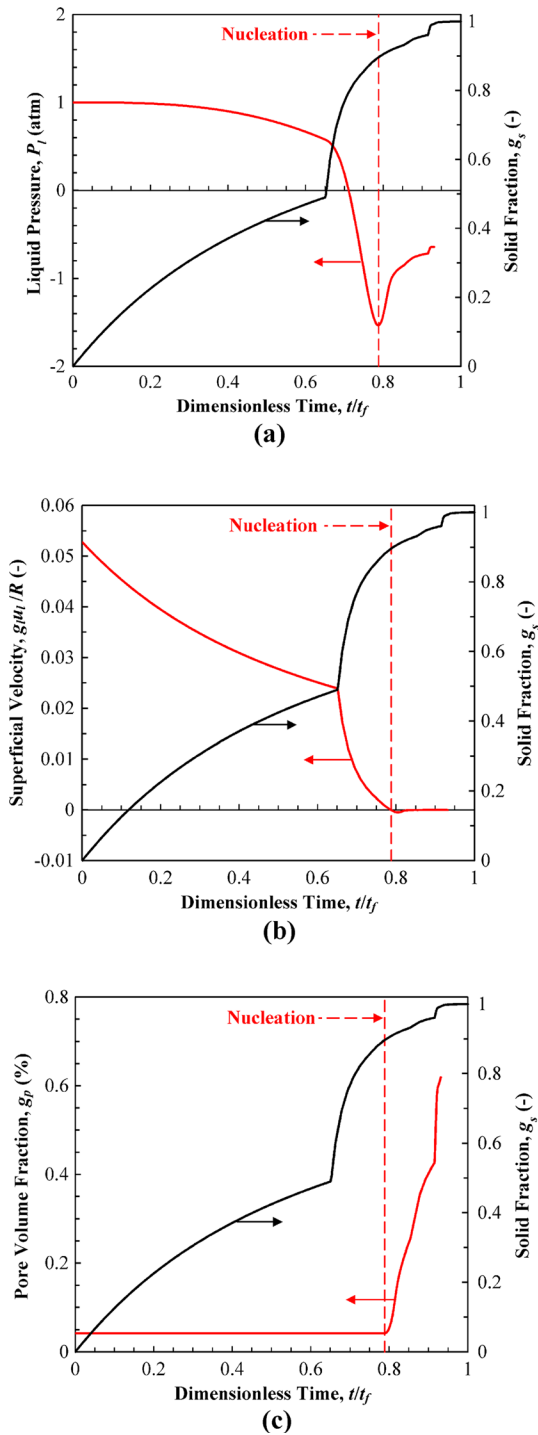
(a)

(b)

(c)

Fig. 5—Simulation results as a function of dimensionless time for pure shrinkage porosity: (*a*) liquid pressure; (*b*) dimensionless superficial velocity; (*c*) pore volume fraction. This simulation uses $\dot{T} = 1$ K/s, $Ny = 0.05$ (K-s)$^{0.5}$/mm, $r_{p,0} = 10$ μm, $n_p = 10^{11}$ m^{-3} (Color figure online).

2. Parametric studies

Parametric studies were performed in order to better understand how, in the case of pure shrinkage, the final pore volume percentage is influenced by differing values of model parameters. The results of the parametric studies are presented in Figure 6, which includes three

plots of the adjusted final pore volume percentage *vs* Niyama value, showing the influence of (a) cooling rate, $\dot{T}$; (b) nucleation pore radius, $r_{p,0}$; and (c) pore number density, n_p. The adjusted final pore volume percentage is defined as the difference between final and initial pore volume percentage values, *i.e.*, $\left(g_p(l) - g_{p,0}\right) \times 100$, where the initial pore fraction is defined as $g_{p,0} = n_p 4\pi r_{p,0}^3 / 3$. This adjustment eliminates the effect of $g_{p,0}$ on the results when n_p and $r_{p,0}$ are varied. Unless otherwise stated in Figure 6, all simulations were performed using the base conditions from the previous subsection.

A high-level overview of the results in Figure 6 reveals that the Niyama value, which ranges over three orders of magnitude across the abscissa of these plots (note the log scale), has a great influence on the adjusted final porosity percentages. Porosity starts to occur at some critical Niyama value [≈ 0.4 (K-s)$^{0.5}$/mm for the base conditions], and steadily increases in magnitude as Niyama decreases below the critical value. Note that the maximum value of the pore volume fraction, as $Ny \rightarrow 0$, is equal to $\beta/(\beta + 1)$ for pure shrinkage.[13] These observations aid in validating both the long-time use of the Niyama criterion by industry to predict shrinkage porosity, as well as the importance placed on this criterion in the present model.

In Figure 6(a), a substantial spread is seen among the three cooling rate value curves, due to the important influence of cooling rate on the liquid pressure drop within the mushy zone, as explained next. Increasing the cooling rate reduces the secondary dendrite arm spacing (see the SDAS equation in Table I), hence reducing the permeability (K) per the Kozeny–Carman equation, Eq. [15]. Thus, prior to nucleation, the magnitude of the negative pressure gradient increases according to Darcy's law (Eq. 14), causing the liquid pressure to drop to the critical nucleation pressure sooner (*i.e.*, at a lower value of t/t_f). Recall from the earlier discussion of the initial shrinkage porosity case, Section III–A–1, that upon nucleation the superficial velocity becomes negative but with a small absolute magnitude because most solidification shrinkage is accommodated by porosity growth rather than by liquid feeding. Given that higher cooling rates cause nucleation to occur earlier (when the liquid volume fraction is higher), the remaining volume of solidification shrinkage is higher, leading to a higher final porosity content.

The influence of nucleation pore radius upon final porosity content is explored in Figure 6(b). Comparing the three curves, it is evident that increasing the nucleation pore radius by a factor of four (from 5 μm to 20 μm) increases the final porosity content, but the effect is relatively small. Much like the case in Figure 6(a), final porosity increases, as nucleation pore radius increases, because nucleation occurs at a lower t/t_f value. However, for the scenario illustrated in Figure 6(b), nucleation occurs earlier because as $r_{p,0}$ increases, the nucleation liquid pressure $P_l = -P_{\sigma,nuc}$ increases (*i.e.*, becomes a smaller negative number), and thus the pore nucleation condition, $P_l \leq -2\sigma/r_{p,0}$,
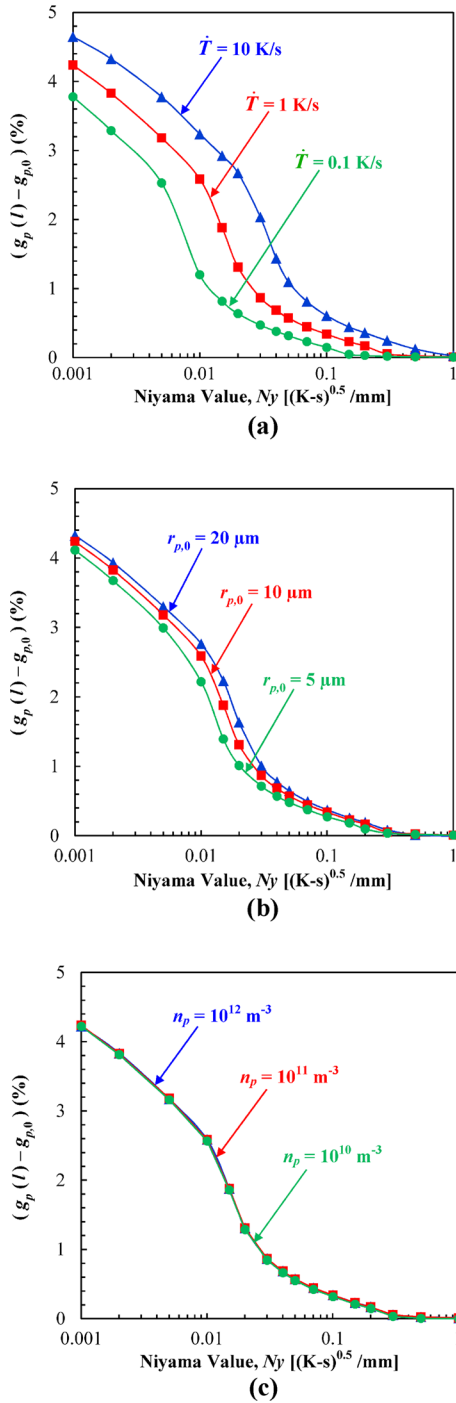
Fig. 6—Adjusted pore volume fraction as a function of the Niyama value for pure shrinkage porosity, showing the effects of (a) cooling rate; (b) nucleation pore radius; and (c) pore number density. The simulations use the following parameters unless otherwise stated on the plots: $\dot{T} = 1$ K/s, $r_{p,0} = 10 \, \mu m$, $n_p = 10^{11} \, m^{-3}$ (Color figure online).

occurs sooner. Earlier nucleation produces a larger final porosity content for the same reasons described in the discussion of Figure 6(a).

The results for the third scenario of the parametric study are plotted in Figure 6(c), which shows that the final adjusted porosity is independent of n_p. This finding is important because for pure shrinkage, as seen in

Figure 1(a), the pores are usually not spherical (unless they are very small), and pore radii and number densities are difficult to identify. The pore volume fraction, on the other hand, is easily measured on a metallographic section. Hence, although the present model is formulated in terms of the spherical pore radius r_p, and the choice of n_p does affect r_p, the predicted pore volume fraction for pure shrinkage, $g_p = n_p 4\pi r_p^3 / 3$, is independent of the assumed pore shape.

3. Comparison of the current model with the Carlson–Beckermann model[13]

This section compares and contrasts both the physical modeling approaches and simulation results generated by the porosity model developed within this research, *vs* an earlier model,[13] referred to henceforth as the C-B model. This comparison is intended to show the difference in model results and explain the reasons for the observed differences. To further explore differences between these models, a simplified version of the current model (termed the "simplified current model") was formulated to confirm the forthcoming explanation of the differing results obtained for the current and C-B models. The simulations were performed using the base conditions from Section III–A–1: $\dot{T} = 1$ K/s, $Ny = 0.05 \, (\text{K-s})^{0.5}/\text{mm}$, $r_{p,0} = 10 \, \mu m$, and $n_p = 10^{11} \, m^{-3}$.

By comparing the mathematical formulations describing each model, it is evident that there are two principal differences between the current and C-B models, specifically:

1. Unlike the current model, the C-B model does not include the pore fraction within its integrated continuity equation; compare Eq. [12] for u_l to the expression in Reference 13: $u_l = R\beta$. In essence, the C-B model assumes an overly high shrinkage flow velocity that is sufficient to feed the entire mushy zone shrinkage volume, without accounting for porosity formation.
2. The C-B model assumes that upon pore nucleation, the feeding flow ceases and the remaining shrinkage is accommodated solely by porosity growth; this assumption is not invoked in the current model.

In an attempt to mimic the C-B model characteristic described in item (2) above, the "simplified current model" mentioned above was created from the current model by stopping liquid flow (*i.e.*, setting $g_l u_l = 0$) upon pore nucleation, thereby leaving the remaining mushy zone shrinkage to be accommodated solely by porosity growth. Consequently, the simplified current model calculates porosity evolution using the following equation:

$$g_p = g_p(l) - \frac{\beta g_l}{1 + \beta} = g_{p,0} + \frac{\beta}{1 + \beta}\left(g_{l,cr} - g_l\right) \quad g_l \leq g_{l,cr}$$

[24]

where $g_{l,cr}$ is the critical liquid fraction at which pores nucleate.

The simulation results for the model comparisons are presented in Figure 7. The ensuing discussion will focus only on describing and explaining the differences between the current model and the C-B model results, while using the simplified current model only to substantiate the findings. Additionally, the discussion will emphasize how the differences between the current and C-B models, enumerated above, produce differing simulation results.

Regarding the difference in continuity equation formulations, explained in item (1) above, the C-B model overestimates the liquid superficial velocity (see Figure 7(b)). The coupling between this velocity and the pressure gradient in Darcy's law thus leads to a steeper downward pressure gradient compared to the current model (see Figure 7(a)). This causes pore nucleation to occur earlier (*i.e.*, at lower t/t_f and lower g_s values) with the C-B model, compared to the current model. Reiterating prior arguments, earlier nucleation at higher residual liquid volume fraction leads to a higher final porosity content, as confirmed in Figure 7(c).

The simulation results for the "simplified current model" largely replicate those for the current model except for minor differences seen following pore nucleation. Since the superficial velocity is assumed to be zero after pore nucleation in the simplified model, Figure 7(b), the liquid pressure is constant after pore nucleation, Figure 7(a). This causes a small difference in the pore volume fraction evolution immediately after nucleation, Figure 7(c), but the final pore volume percentages resulting from the current model and the simplified current model are nearly identical. This implies that the difference in the treatment of superficial velocity after nucleation (*i.e.*, item 2) does not have a noticeable impact on the final pore volume.

In conclusion, the comparison of the C-B simulation results to the two alternatives of the current model shows that the more precise treatment of continuity by the current model (see item 1 above) is the dominant factor that distinguishes the more accurate current model from the baseline C-B model. The price for this improvement is that in the current model, an iterative prediction-correction algorithm is required to determine $g_p(l)$ (see Section II–E).

It is shown in Reference 13 that if the predicted shrinkage porosity volume fraction is plotted against a properly non-dimensionalized Niyama value, a curve results that is universal for a given alloy. The dimensionless Niyama value is defined as

$$Ny* = C_\lambda \dot{T}^{-1/3} Ny \sqrt{\frac{P_{atm} + 2\sigma/r_{p,0}}{\mu_l \beta \Delta T_f}} \qquad [25]$$

where ΔT_f is the freezing temperature range of the alloy. Figure 8 shows a comparison of the adjusted final pore fractions predicted by the current model and the C-B model, plotted against $Ny*$. It can be seen that for any given dimensionless Niyama value, the porosity predicted by the C-B model is larger than that predicted by the current model. As discussed in conjunction with
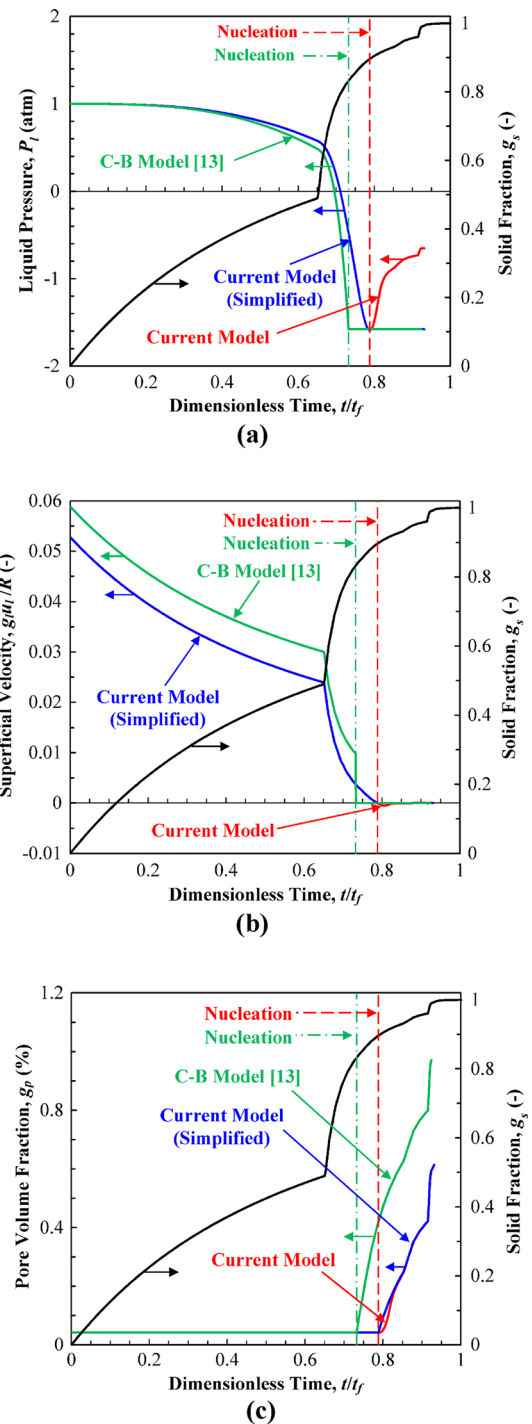

Fig. 7—Comparison of three different models for pure shrinkage porosity: 1- Current Model; 2- Current Model (Simplified); 3- C-B Model.[13] In the simplified current model, it is assumed that after pore nucleation, the liquid velocity vanishes: (*a*) liquid pressure; (*b*) dimensionless superficial velocity; (*c*) pore volume fraction. The simulations use $\dot{T} = 1$ K/s, $Ny = 0.05$ (K-s)$^{0.5}$/mm, $r_{p,0} = 10\,\mu$m, $n_p = 10^{11}$ m^{-3} (Color figure online).

Figure 7, this is because the liquid pressure drops faster in the C-B model than in the current model, and thus pore nucleation occurs earlier, and consequently the final pore fraction becomes larger. The difference between the two model predictions is largest at

intermediate $Ny*$ values, but does not exceed a pore volume percentage of 1 pct (absolute). Note, however, that the critical dimensionless Niyama value at which porosity starts to form is the same in both models ($Ny* \approx 100$). The predicted pore fraction as $Ny* \rightarrow 0$ is also the same. Clearly, the curve obtained from the current model must be considered more accurate, since it accounts for the effect of porosity on the feeding flow.

B. Combined Gas and Shrinkage Porosity

First, two simulations are presented here to examine in detail the time evolution of the various variables in the model for the case of combined gas- and shrinkage-induced porosity. Both use a moderate gas content of $C_0 = 0.20$ cc/100 g and common model parameters: $\dot{T} = 1$ K/s, $r_{p,0} = 10\ \mu m$, $n_p = 10^{11}$, and $m = 3$. The only difference between the two simulations is the Ny value; for Case 1, $Ny = 5.0\,(\text{K-s})^{0.5}/\text{mm}$; and for Case 2, $Ny = 0.05\,(\text{K-s})^{0.5}/\text{mm}$. Although shrinkage-induced porosity is negligibly small in Case 1, it is included in this section to allow for a better understanding of Case 2, where gas and shrinkage both contribute to pore growth. The discussion of these two cases is followed by a closer examination of the Blake singularity as well as by extensive parametric studies.

1. Case 1: pure gas porosity

Case 1, with $Ny = 5.0\,(\text{K-s})^{0.5}/\text{mm}$, represents a situation in which the dissolved gas is the dominant mechanism in porosity formation and growth, but the Ny value is sufficiently high that shrinkage-induced porosity is negligibly small (see Figure 6). The results of this simulation are provided in Figure 9; as in the pure shrinkage results, the variables of interest are plotted against dimensionless time, and each plot includes the solid fraction for reference. As shown in Figure 9(a), the liquid pressure decreases only very slightly during solidification, except for a sharper drop at the very end of solidification. The fact that the liquid remains essentially at atmospheric pressure is typical of pure gas porosity. In contrast, the pore pressure, Figure 9(b), increases appreciably throughout solidification in accordance with Sievert's law, due to solute accumulation in the liquid melt, as seen in Figure 9(d). The pore pressure begins to increase very sharply once the primary eutectic phase begins to form (at $t/t_f = 0.65$), and this steep increase in pore pressure continues until porosity nucleates shortly thereafter (at $t/t_f = 0.67$) because P_p becomes large enough to satisfy the pore nucleation condition, Eq. [5]. Once pore nucleation occurs, the elevated pore pressure drops, relieved by pore growth in accordance with Eq. [1]. Examining the plots in Figure 9, note that care must be taken to distinguish the influences of nucleation from those related to the fraction solid discontinuity associated with the initial eutectic phase formation, particularly given the short time interval between these two significant events. The superficial velocity, shown in Figure 9(c), decreases during solidification in a manner similar to that of the pure shrinkage case (see Figure 5(b)). However, in this
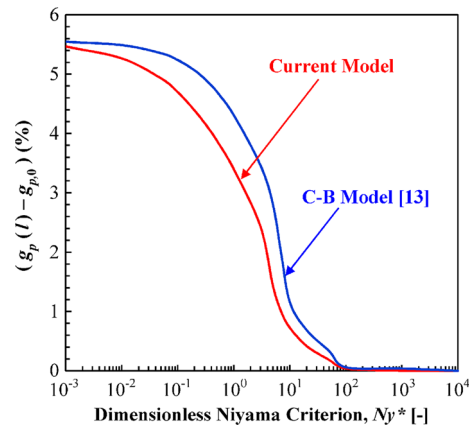

Fig. 8—Predicted final adjusted pore volume fraction as a function of the dimensionless Niyama criterion for pure shrinkage porosity in an A356 aluminum alloy: comparison of the current model with the C-B model[13] (Color figure online).

instance it decreases more slowly, dropping to zero only at the end of solidification, and never becoming negative. Most importantly, the liquid velocity has a significant magnitude during pore growth, unlike the case of pure shrinkage. This indicates that the growth of the pore compensates only some of the solidification shrinkage. The continuous infusion of gas-solute into the liquid at the solidification front causes the gas solute concentration in the liquid, C_l, to increase throughout solidification, as shown in Figure 9(d). The noteworthy increase in the slope of C_l where the primary eutectic phase begins to form is the result of the corresponding rapid increase in the rate of solid formation (see the solid fraction curve), which in turn causes a rapid increase in the rate of gas solute rejection into the liquid at the solidification front. When porosity nucleates, gas-solute diffuses into the pores, which simultaneously increases pore radius (Figure 9(e)), decreases pore pressure (Figure 9(b)), and lowers the equilibrium solute concentration at the pore-liquid interface, C_{lp} (Figure 9(d)), in accordance with Sievert's law. The evolution of the pore volume in this simulation is shown in Figure 9(f). The pore volume increases steadily to a value of 0.31 pct at the end of solidification. Note that, all the results in Figure 9 show a noticeable change in slope near the end of solidification, corresponding to the beginning of Mg_2Si phase formation. Unlike the pure shrinkage results shown in Figure 5, however, the slope changes in the present simulation have little effect on the final pore volume seen in Figure 9(f).

2. Case 2: combined gas and shrinkage porosity

For this case, all model inputs are identical to those of Case 1, except that the Niyama value has been reduced by two orders of magnitude to $Ny = 0.05\,(\text{K-s})^{0.5}/\text{mm}$. The combination of moderate gas level and low Niyama value produces a case in which both hydrogen diffusion and solidification shrinkage simultaneously influence porosity evolution. Inspection of the results for Case 2, shown in Figure 10, reveals that each plot exhibits a discontinuity (spike or a curve perturbation) in the
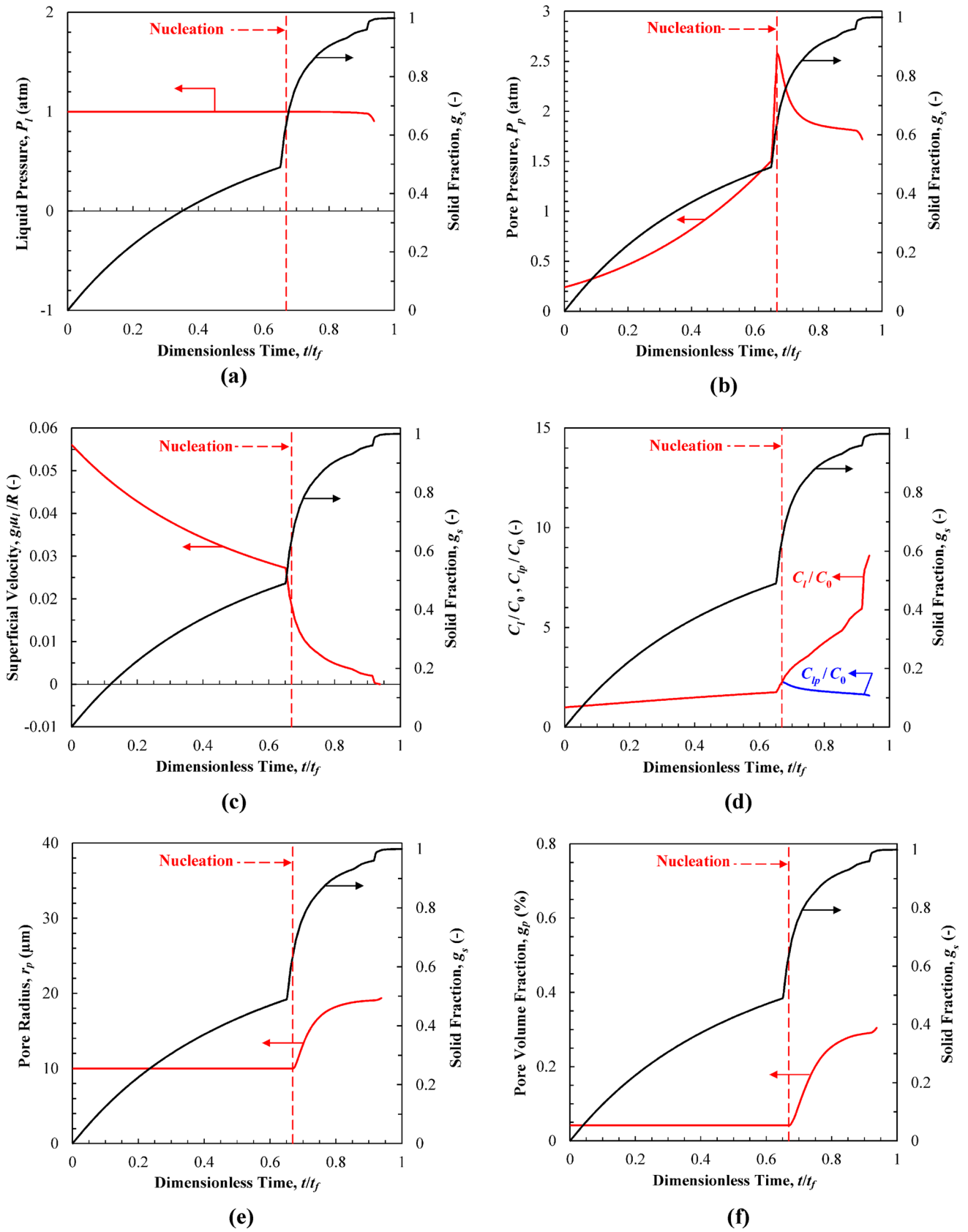
Fig. 9—Simulation results as a function of dimensionless time for pure gas porosity: (*a*) liquid pressure; (*b*) pore pressure; (*c*) dimensionless superficial velocity; (*d*) gas concentration in the melt and equilibrium gas concentration; (*e*) pore radius; (*f*) pore volume fraction. This simulation uses $C_0 = 0.20 \, cc/100 \, g$, $Ny = 5 \, (K\text{-}s)^{0.5}/mm$, $\dot{T} = 1 \, K/s$, $r_{p,0} = 10 \, \mu m$, $n_p = 10^{11} \, m^{-3}$, $m = 3$ (Color figure online).

vicinity of $t/t_f \approx 0.75$, (*i.e.*, within the blue shaded bands). These perturbations are related to the Blake singularity and will be addressed in the next section (Section III–B–3). In the present section, attention is focused on the portion of the plots to the left and right of the shaded bands.

The plots in Figure 10 for Case 2 display similar trends to those seen in Figure 9 for Case 1, neglecting for the moment the perturbations within the shaded zones of Figure 10, except for one important difference. Due to the low Niyama value in Case 2, the liquid pressure drop across the mushy zone is significantly larger than in Case 1 (Figures 9(a) and 10(a)). Recalling the pore nucleation condition expressed in Eq. [5], note that prior to pore nucleation, both the falling liquid pressure (Figure 10(a)) and the rising pore pressure (Figure 10(b)) favor nucleation. However, nucleation occurs only slightly earlier in Case 2 than in Case 1, because in both cases the rise in pore pressure that occurs upon formation of the primary eutectic phase is very steep. The combined behaviors of the liquid and pore pressures do, however, have a significant impact upon the final pore volume; note from Figure 10(f) that the final pore volume of 1.22 pct is about four times larger than the purely gas-driven result in Figure 9(f), and about twice as large as the pure shrinkage value seen in Figure 5(c). This can be understood by considering the variables presented in Figure 10. First, the liquid pressure falls significantly before porosity nucleates. When porosity nucleates, mechanical equilibrium dictates that the pore pressure is bound by Eq. [1], which results in a much lower pore pressure after nucleation for Case 2 than for Case 1 in Figure 9(b). The lower pore pressure after nucleation in Case 2 results in a lower equilibrium concentration, C_{lp}, according to Eq. [20]. This results in a larger value of $(C_l - C_{lp})$, which according to Eq. [19] results in a larger mass diffusion rate of gas solute into pores, thus producing faster growing pores according to Eq. [4]. Since the pore number density is a constant parameter, larger pores lead to a larger pore volume. Finally, since the liquid concentration, C_l, is a function of the pore volume (see Eq. [22]), increasing the pore volume increases C_l, which further increases $(C_l - C_{lp})$ in Eq. [19]. The end result is that for comparable parameters, this "mixed-mode" pore growth case can result in larger porosity values than either the pure shrinkage case or the gas-driven case.

3. Blake singularity

The Blake singularity, first mentioned in Section II–A, refers to the potential for unbounded pore growth and collapse rates when the denominator of the term outside of the brackets on the RHS of Eq. [4] goes to zero, *i.e.*, at the Blake criterion pressure $P_l = -4\sigma/3r_p$ or, equivalently, $3r_pP_l + 4\sigma = 0$. Figure 11 confirms that the value of the denominator drops rapidly when $t/t_f \approx 0.741$, becomes negative and rises above zero, only to gradually regress to low, yet positive levels. The calculated pore radius (Figure 10(e)) during the singularity experiences first a rapid increase followed by an equally rapid decrease to about the same magnitude as before the singularity. This behavior is indicative of bubble cavitation.[19]

During simulations in which the Blake singularity occurred, an extremely small time step was used in an attempt to resolve the rapid changes associated with the singularity. In addition, a tiny number (10^{-20}) was added to the denominator in order to avoid a floating point exception. Since after the singularity region, all variables return to approximately the same values as before the singularity, the simulations involving a singularity were still deemed reliable. A Blake singularity was never observed in simulations for pure shrinkage- or pure gas-induced porosity. It only occurred in simulations involving combined gas- and shrinkage-driven pore growth. The parameter ranges where the Blake singularity occurs are provided in the next subsection.

The authors are not aware of experimental studies where pore cavitation was observed during solidification of metal alloys. It is important to realize that the rapid transients associated with cavitation are not properly modeled in the present study. During bubble cavitation, phenomena such as the inertia of the fluid surrounding a pore must be taken into account.[19] Furthermore, the present model assumes a quasi-steady diffusion boundary layer for the gas species around a pore, which is clearly inappropriate for rapid changes in the pore radius. Hence, the details of the calculated variations of the variables in the shaded bands of the plots in Figure 10 cannot be considered realistic.

4. Parametric studies

Parametric studies using simulations with a gas solute content greater than zero have been carried out to elucidate the effect of modeling parameters upon the adjusted final porosity content, similar to the parametric studies reported earlier for pure shrinkage porosity in Section III–A–2. Adjusted final porosity results from these simulations are presented in Figure 12. Similar to the earlier results for pure shrinkage porosity, the Niyama value, Ny, represented in log-scale on the abscissa of each plot, has the greatest influence on the final pore content for all five plots in Figure 12. As explained in connection with Figure 6, the final porosity increases as the Niyama value decreases. Figure 12(a) illustrates the effect that the initial melt gas concentration has on the final porosity values. As expected, for any given Niyama value, the final pore fraction increases as the initial melt hydrogen gas concentration increases. However, unlike the pure shrinkage results in Figure 6, the pore fraction in the presence of dissolved gas no longer vanishes for $Ny \geq 0.4 \, (\text{K-s})^{0.5}/\text{mm}$, but rather approaches a constant value. The finite pore fraction values predicted at high Ny in Figure 12(a) represent pure gas porosity, without any shrinkage contribution. As $Ny \rightarrow 0$, the curves for all initial gas contents converge to the same value, indicating that shrinkage dominates. Note that the curves for $C_0 = 0.01$ and $0.1 \, \text{cc}/100 \, \text{g}$ in Figure 12(a) are very close to each other, and the curve for $C_0 = 0.01 \, \text{cc}/100 \, \text{g}$ is nearly identical to the pure shrinkage curve in Figure 6(a). Hence, gas levels below about $0.1 \, \text{cc}/100 \, \text{g}$ hydrogen in this A356 alloy have little or no effect on porosity formation. Similar threshold gas levels for porosity in alloy
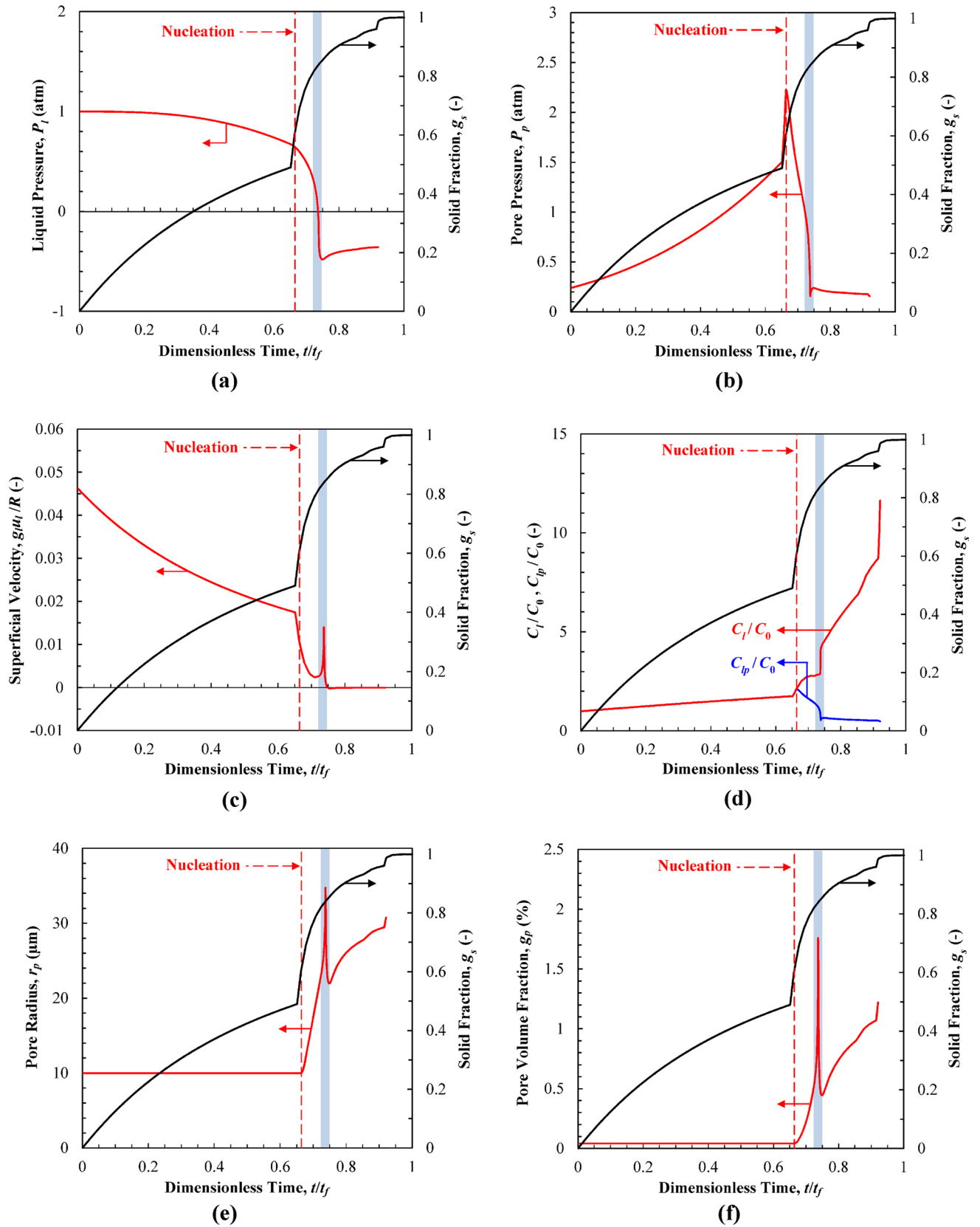
Fig. 10—Simulation results as a function of dimensionless time for combined shrinkage and gas porosity: (*a*) liquid pressure; (*b*) pore pressure; (*c*) dimensionless superficial velocity; (*d*) gas concentration in the melt and equilibrium gas concentration; (*e*) pore radius; (*f*) pore volume fraction. This simulation uses $C_0 = 0.2$ cc/100 g, $Ny = 0.05$ (K-s)$^{0.5}$/mm, $\dot{T} = 1$ K/s, $r_{p,0} = 10 \mu$m, $n_p = 10^{11}$ m^{-3}, $m = 3$. The blue-shaded bands indicate the Blake (cavitation) singularity (Color figure online).
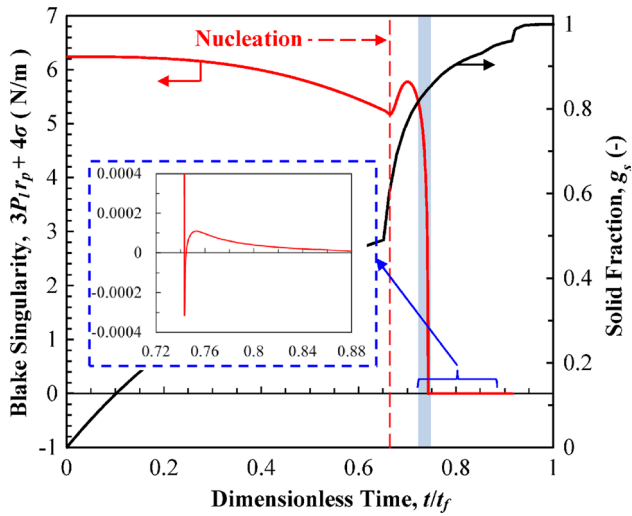
Fig. 11—Variation of the Blake singular term with dimensionless time for the simulation of Fig. 10 (Color figure online).

ordinate in Figure 12(c) largely negates the effect of nucleation pore radius, much in the same way observed in Figure 6(b). As a consequence, the curves on this plot (which represent a four-fold increase of nucleation pore radius) exhibit only a slight increase in the final porosity content, in contrast to the significant influence of the Niyama value that is represented on the abscissa of this plot.

Figure 12(d) examines how varying the pore number density, *i.e.*, $n_p = 10^{10}$, 10^{11} and 10^{12} m^{-3}, influences the final porosity content. For low Niyama values, porosity is governed predominantly by shrinkage, and it was already shown in connection with Figure 6 that in this regime, n_p has no effect on $(g_p(l) - g_{p,0})$. For high Niyama values, greater than about 0.5 (K-s)$^{0.5}$/mm, the final porosity generally decreases as pore number density increases. As the pore number density increases, each pore will contain less gas, pores will be smaller, and pore capillary pressure will be higher. Thus, final pore volume fraction will be lower as pore number density increases. Note that, this trend is somewhat obscured in Figure 12(d) because of the use of the adjusted pore fraction on the abscissa.

Figure 12(e) investigates the effect of the choice of the exponent *m* in the impingement factor, $\varphi = (1 - g_s)^m$, on the predicted final pore fraction. The impingement factor attempts to estimate the ''effective'' pore-liquid interfacial area, A_p, in the mass diffusion rate described by Eq. [18], in order to account for the fact that part of the pore will be in contact with solid rather than liquid. Simulation results indicate that when Niyama values are low (*e.g.*, $Ny < \sim 0.01$ (K-s)$^{0.5}$/mm) the impingement factor has almost no influence on the final porosity content. This is to be expected, given that in this Niyama value regime, porosity formation is controlled by solidification shrinkage. Conversely, as the Niyama value progressively increases above this threshold, the final porosity content is increasingly influenced by gas-solute transport and thus by the exponent ''m'' in the impingement factor equation. Figure 12(e) indicates that as the exponent increases, the final porosity content decreases. This is because a larger exponent value yields a lower impingement factor value, which corresponds to a lower ''effective'' pore-liquid interfacial area through which gas can diffuse, hence producing a lower final porosity content.

solidification are well known in the literature, *e.g.*, Reference 14. The blue-shaded region in Figure 12(a) indicates the ranges of Niyama and initial gas content where a Blake singularity was observed in the simulations. The singularity always occurs when the Niyama value is low enough and the initial gas content is high enough that both shrinkage and gas diffusion play a significant role. Note that, the curves in the blue-shaded region in Figure 12(a) are smooth and have a similar shape as the one for pure shrinkage, lending further support to the validity of the results that displayed a Blake singularity.

Figure 12(b) displays an interesting phenomenon regarding the relationship between cooling rate, Niyama value, and the final pore volume. For low Niyama values ($Ny < 0.04$ (K-s)$^{0.5}$/mm), increasing the cooling rate causes an increase in the final pore fraction, while for higher Niyama values ($Ny > 0.1$ (K-s)$^{0.5}$/mm), the opposite trend is observed. This trend reversal is caused by the differing balance between shrinkage and gas diffusion porosity drivers. At low Niyama values, where solidification shrinkage is the dominant pore growth mechanism, a cooling rate increase fosters a larger liquid pressure drop, thereby resulting in earlier pore nucleation at higher volume fraction liquid, leading to higher final porosity content. On the other hand, for higher Niyama values, gas-solute diffusion regulates pore growth, and thus increasing the cooling rate reduces the time available for mass transport to the growing pores, which subsequently decreases the final adjusted porosity content. Between these two extremes (*i.e.*, $0.04 < Ny < 0.1$ (K-s)$^{0.5}$/mm) is a transition region separating the two pore growth regimes.

The nucleation pore radius parametric study results are given in Figure 12(c). Clearly, a larger initial pore radius ($r_{p,0}$) reduces the nucleation capillary pressure, $P_{\sigma,nuc} = 2\sigma/r_{p,0}$, which leads to earlier pore nucleation and a higher porosity level ($g_{p,0}$). However, the use of the adjusted pore fraction ($g_p(l) - g_{p,0}$) as the plot

C. Model Calibration for Pure Gas Porosity

Although the simulation results presented thus far have shown that the porosity model generates physically reasonable results and trends over a wide range of parameters, it is also important to gauge the porosity model simulations against experimental data. However, the model contains a number of parameters (*e.g.*, impingement factor, pore number density, and nucleation pore radius) that are difficult to determine by direct experimental measurement; the model also uses thermophysical properties (*e.g.*, diffusivities, partition coefficients, and viscosities) that are prone to uncertainty. Given the dearth of relevant experimental
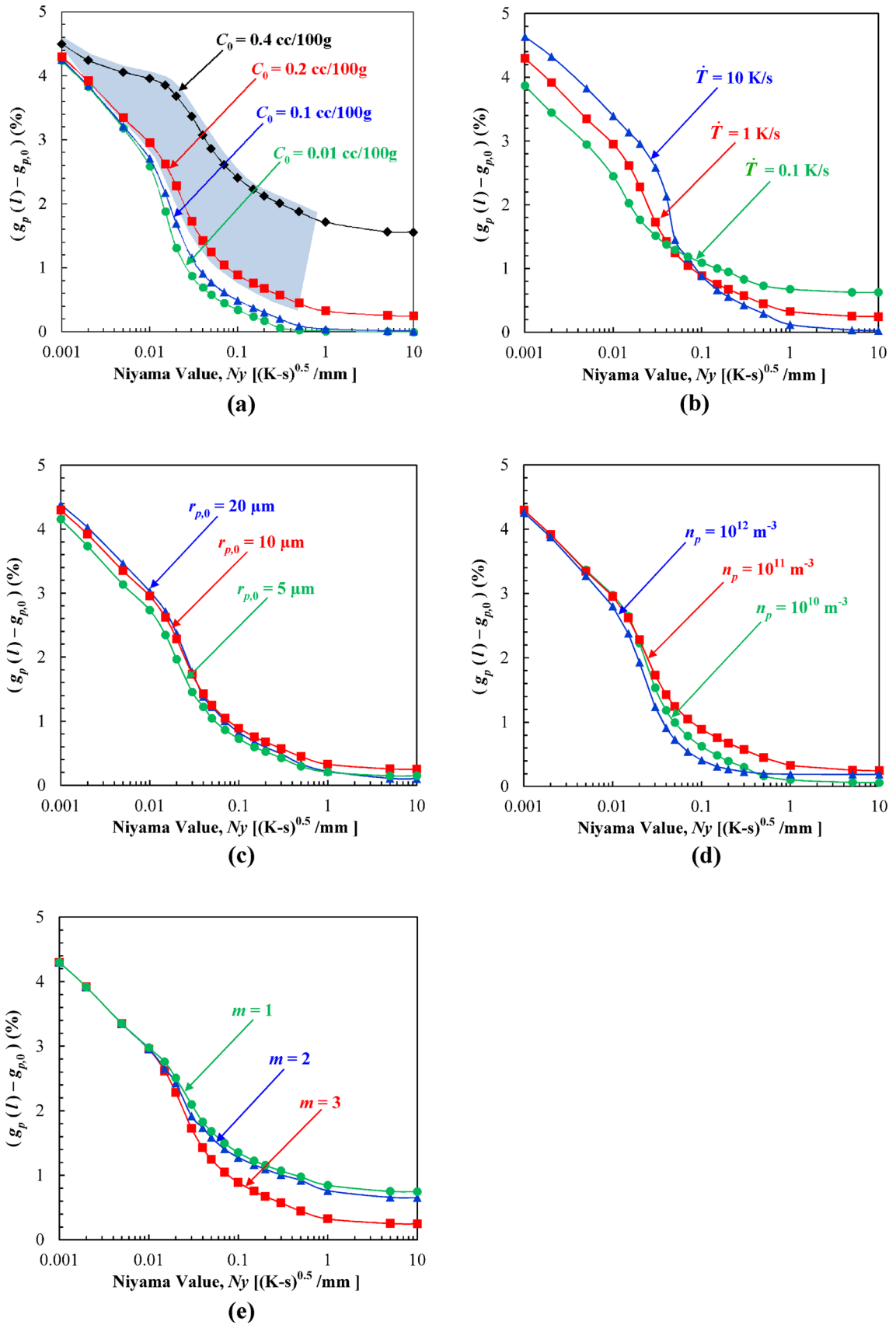
Fig. 12—Adjusted pore volume fraction as a function of the Niyama value for combined shrinkage and gas porosity, showing the effects of (*a*) initial gas concentration [the blue shaded band indicates the parameter regime where the Blake (cavitation) singularity occurs]; (*b*) cooling rate; (*c*) nucleation pore radius; (*d*) pore number density; and (*e*) impingement factor exponent. The simulations use the following parameters unless otherwise stated on the plots: $C_0 = 0.20\,\mathrm{cc}/100\,\mathrm{g}, \dot{T} = 1\,\mathrm{K/s}, r_{p,0} = 10\,\mu\mathrm{m}, n_p = 10^{11}\,\mathrm{m}^{-3}, m = 3$ (Color figure online).

porosity data available in the literature, this model calibration focuses on the influence of the cooling rate upon the final pore volume fraction, $g_p(l)$, with the impingement factor exponent, m, and pore number density, n_p, as the main calibration factors. Subsequently, the effect of the nucleation pore radius, $r_{p,0}$, is investigated.

Two sets of experimental porosity data, available within the literature,[23,24] are used in the calibration of the present porosity model. The experimental data are for an A356 aluminum alloy with two different initial hydrogen solute concentrations in the melt, $C_0 = 0.13$ cc/100 g and $C_0 \approx 0.26$ cc/100 g. In all experiments, the alloy was solidified directionally under thermal conditions that produced a common Niyama value of $Ny = 3.265 \, (\text{K-s})^{0.5}/\text{mm}$.[14] This Niyama value is sufficiently large that the porosity is purely gas driven; nonetheless, the simulations were performed with the full model. The experimental and corresponding simulation results are shown in Figures 13 through 15, which display the final pore volume fraction as a function of inverse cooling rate ($1/\dot{T}$). The overall trend of the data for both gas concentrations is that the pore fraction increases as the inverse cooling rate increases (*i.e.*, as the cooling rate decreases). This effect can be directly attributed to finite rate gas diffusion.[14]

1. *Calibration trial exploring the effect of impingement factor exponent*

The first calibration trial compares the experimental data to simulation results generated using two different impingement factor exponents: $m = 2$ and $m = 3$. For this trial, the pore number density and the nucleation pore radius are set to $n_p = 10^{11}$ m^{-3} and $r_{p,0} = 10 \, \mu$m, respectively. Figure 13 illustrates that the predicted final pore percentage decreases significantly as the value of m increases from $m = 2$ to $m = 3$, which agrees with the findings and the explanation presented earlier relative to Figure 12. However, neither $m = 2$ nor $m = 3$ does particularly well in matching the experimental results. For the low C_0 data (Figure 13(a)), the two simulated pore percentage curves straddle the data, whereas for the higher C_0 data (Figure 13(b)), both simulations over-predict the final porosity content.

2. *Calibration trial exploring the effect of pore number density*

The second calibration trial, shown in Figure 14, compares the experimental data to simulation results for two different pore number densities: $n_p = 10^{10}$ m^{-3} and $n_p = 10^{11}$ m^{-3}. For this trial, the impingement factor and initial pore radius are set to $m = 3$ and $r_{p,0} = 10 \, \mu$m, respectively. For the lower initial gas concentration results, Figure 14(a) indicates that $n_p = 10^{11}$ m^{-3} produces results closer to the experimental data than $n_p = 10^{10}$ m^{-3}. The $n_p = 10^{11}$ m^{-3} results in this plot agree with experimental data for low inverse cooling rates, but the porosity values do not increase with rising inverse cooling rate as quickly as do the experimental measurements. Conversely, for the higher initial gas
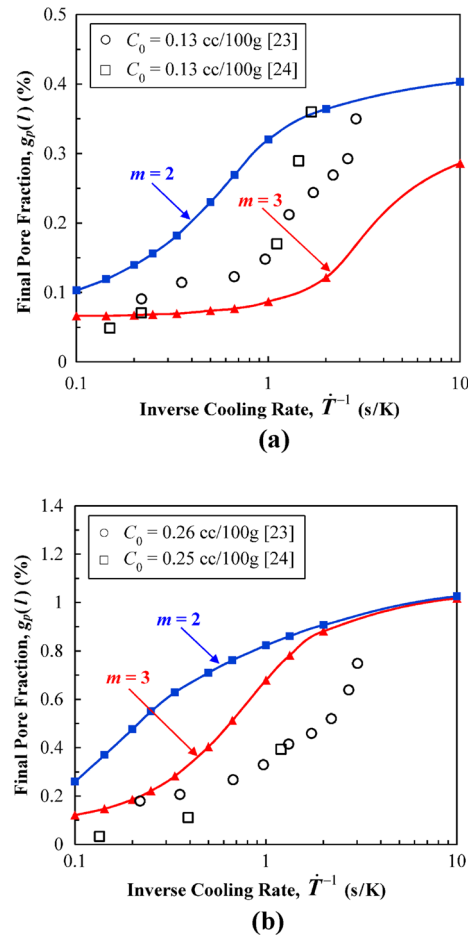

Fig. 13—Comparison of measured and predicted pore volume fractions as a function of inverse cooling rate, showing the effect of the impingement factor exponent: (*a*) $C_0 = 0.13$ cc/100 g; (*b*) $C_0 = 0.26$ cc/100 g. The simulations use $Ny = 3.265 \, (\text{K-s})^{0.5}/\text{mm}$, $r_{p,0} = 10 \, \mu$m, $n_p = 10^{11}$ m^{-3} (Color figure online).

concentration results, Figure 14(b) shows that the $n_p = 10^{10}$ m^{-3} results are in better agreement with experimental results than for $n_p = 10^{11}$ m^{-3}.

3. *Final calibration*

Based on the results in the previous two subsections, a final calibration of the porosity model was performed by simultaneously changing the values for pore number density, n_p, and impingement factor exponent, m. Again, the nucleation pore radius is kept at $r_{p,0} = 10 \, \mu$m. Figure 15 (red curves) shows that good overall agreement between measured and predicted pore volume fractions is obtained with $r_{p,0} = 10 \, \mu$m using a single impingement factor exponent of $m = 2.5$ for both gas concentrations, $n_p = 10^{11}$ m^{-3} for $C_0 = 0.13$ cc/100 g, and $n_p = 2 \times 10^9$ m^{-3} for $C_0 \approx 0.26$ cc/100 g. Using the same impingement factor exponent for both initial gas concentrations is reasonable, given that m should not be a function of the amount of dissolved gas. The values obtained in the final calibration trial for the pore number density are, however, different for the two gas
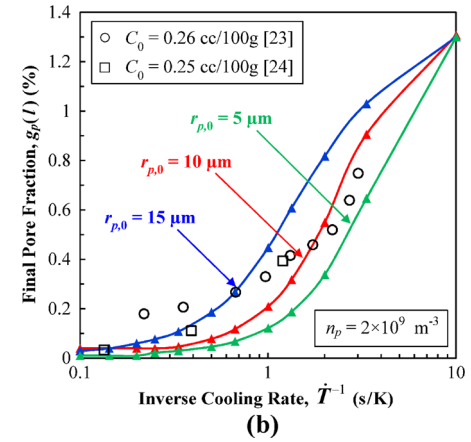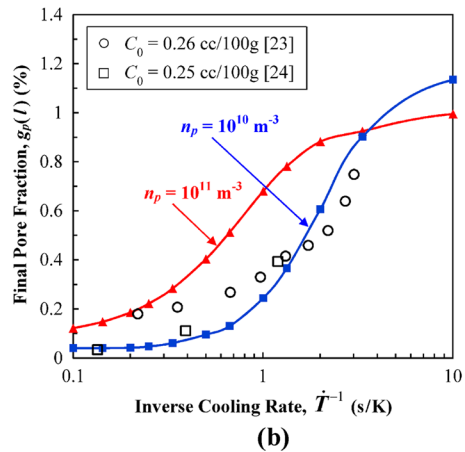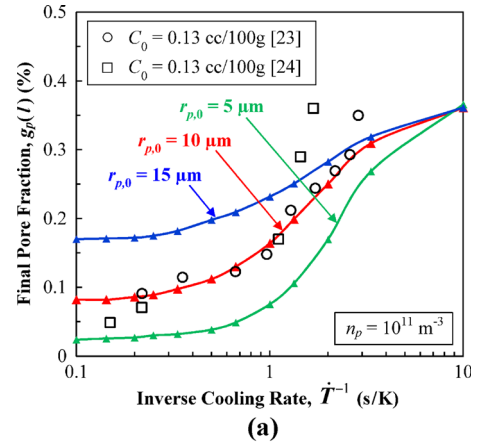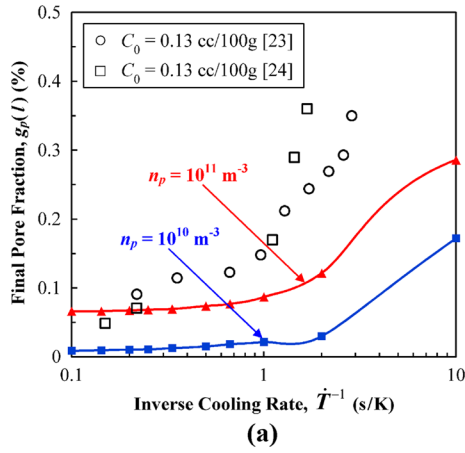
(a)

(b)

Fig. 14—Comparison of measured and predicted pore volume fractions as a function of inverse cooling rate, showing the effect of the pore number density: (*a*) $C_0 = 0.13\,\text{cc}/100\,\text{g}$; (*b*) $C_0 = 0.26\,\text{cc}/100\,\text{g}$. The simulations use $Ny = 3.265\,(\text{K-s})^{0.5}/\text{mm}$, $r_{p,0} = 10\,\mu\text{m}$, $m = 3$ (Color figure online).

(a)

(b)

Fig. 15—Comparison of measured and predicted pore volume fractions as a function of inverse cooling rate, showing the effect of the nucleation pore radius: (*a*) $C_0 = 0.13\,\text{cc}/100\,\text{g}$; (*b*) $C_0 = 0.26\,\text{cc}/100\,\text{g}$. The simulations use $Ny = 3.265\,(\text{K-s})^{0.5}/\text{mm}$, $m = 2.5$, and the pore number densities noted on the plots (Color figure online).

concentrations. For the lower dissolved gas content, the pore fractions are relatively low, the pore radii small, and the pore number density high. Conversely, a higher gas content results in larger pore volume fractions and pore radii, while the pore number density is lower. While this finding appears to be physically reasonable, the variation of the pore number density with the dissolved gas content suggests that a separate model is needed for this dependency. Furthermore, the comparison in Figure 15(b) indicates that even better agreement could be obtained by making the pore number density a function of the cooling rate.

4. Effect of nucleation pore radius

The results of a parametric study showing the effect of variations in the nucleation pore radius, $r_{p,0}$, are also shown in Figure 15. Here, n_p and m are kept at their final calibrated values, and $r_{p,0}$ is varied from 5 to 15 μm. Figure 15(a) reveals that for the lower initial gas concentration, the predicted pore volume fractions for

$r_{p,0} = 15\,\mu$m are much too high for all but the lowest cooling rates. This can be attributed to the fact that with the present value of n_p, the initial pore fraction, $g_{p,0} = n_p 4\pi r_{p,0}^3/3$, is too high when using $r_{p,0} = 15\,\mu$m. In other words, for the higher cooling rates in Figure 15(a), the pores are likely smaller than 15 μm in radius. For the higher initial gas concentration (Figure 15(b)), this effect is not apparent because n_p is much lower. For $r_{p,0} = 5\,\mu$m, on the other hand, Figures 15(a) and (b) both show that the predicted pore fractions remain near zero for inverse cooling rates up to about 0.7 s/K (or cooling rates above 1.43 K/s). This trend is clearly not supported by the experimental data, which show that significant gas porosity can be present at higher cooling rates. For such a low initial pore radius, the nucleation barrier for pores is too high. In conclusion, an intermediate value for the nucleation pore radius of $r_{p,0} = 10\,\mu$m, as used in the final calibration, is the most realistic choice for the present set of experimental data.

IV. CONCLUSIONS

A unified model has been developed for combined gas- and shrinkage-induced pore formation during solidification of metal alloys. The model is based on a pore-centric approach, in which an ordinary differential equation is solved for the evolution of the pore radius as a function of cooling rate, thermal gradient, dissolved gas diffusion, solidification shrinkage, and relevant alloy and gas properties. This formulation allows it to be solved locally, at any point in a casting, as part of a regular casting simulation. Compared with existing local models, the present model features a more accurate treatment of the continuity equation that takes into account the effect of the forming porosity on the liquid velocity in the mushy zone. The present pore-centric approach has allowed for the identification of a Blake instability in pore formation during solidification of metal alloys. This instability leads to unbounded pore growth and collapse, as in bubble cavitation; however, this phenomenon requires additional modeling attention beyond the present treatment. The Blake instability occurs whenever the porosity is induced by both gas and shrinkage.

The model has been exercised in detail, in order to explore the effect of solidification conditions and model parameters on the predicted porosity for an A356 aluminum alloy. The parametric studies reveal how pore volume depends on the Niyama value, melt gas content, cooling rate, and other input parameters. The simulations show that the porosity transitions smoothly from pure shrinkage to pure gas porosity (or no porosity, if the melt gas content is below a certain threshold value) as the Niyama value is increased. For pure shrinkage porosity, a revised dimensionless Niyama curve for the A356 aluminum alloy is presented. For pure gas-induced porosity, a calibration of the model is performed using measurements available in the literature. The experimental trend that the pore volume fraction decreases with increasing cooling rate is well predicted by the model, since it accounts for finite rate gas diffusion.

There are three model input parameters that are difficult to specify: $r_{p,0}$, m, and n_p. The comparison with experimental porosity measurements for an A356 alloy shows that a reasonable value of around 10 μm should be used for the nucleation pore radius, $r_{p,0}$; otherwise, the initial pore volume fraction can be too large (for higher $r_{p,0}$) or the nucleation barrier for pores can be too high (for lower $r_{p,0}$). A similar value for $r_{p,0}$ can be expected to hold for other alloys (*e.g.*, cast steel). The impingement factor exponent, m, and the pore number density, n_p, only play a role for gas porosity. The preliminary calibration study for A356 suggests that $m = 2.5$ works well for any melt gas content and cooling rate. This value for m can also be expected to hold for other alloys, but additional experimental confirmation is needed. However, the pore number density, n_p, is shown to be a function of the melt gas content and a separate model for this dependency is needed. Clearly, the pore number density can also depend on the casting alloy and additional research is needed.

When using the model in a casting simulation, it should be solved as part of the regular solidification calculations. Then, the assumption of a constant cooling rate and thermal gradient is not needed, *i.e.*, these variables can be updated during the time stepping. Other assumptions, such as constant properties and a fixed pressure at the liquidus isotherm, could be easily relaxed as well. However, such modifications would require a new prediction-correction algorithm for $g_p(l)$. In addition, a more efficient numerical algorithm should be developed to allow for larger time steps in the porosity calculations and to deal with the Blake instability.

REFERENCES

1. T.S. Piwonka and M.C. Flemings: *Trans. AIME*, 1966, vol. 236, pp. 1157–65.
2. K. Kubo and R.D. Pehlke: *MTB*, 1985, vol. 16, pp. 359–66.
3. A.S. Sabau and S. Viswanathan: *Metall. Mater. Trans. B*, 2002, vol. 33B, pp. 243–55.
4. Ch. Pequet, M. Rappaz, and M. Gremaud: *Metall. Mater. Trans. A*, 2002, vol. 33A, pp. 2095–2106.
5. P.D. Lee and J.D. Hunt: *Acta Mater.*, 1997, vol. 45, pp. 4155–69.
6. R.C. Atwood, S. Sridhar, W. Zhang, and P.D. Lee: *Acta Mater.*, 2000, vol. 48, pp. 405–17.
7. R.W. Hamilton, D. See, S. Butler, and P.D. Lee: *Mater. Sci. Eng. A*, 2003, vol. 343, pp. 290–300.
8. P.D. Lee and J.D. Hunt: *Modeling of Casting, Welding, and Advanced Solidification Processes VII*, TMS, Warrendale, PA, 1995, pp. 585–92.
9. P.D. Lee and J.D. Hunt: *Scripta Mater.*, 1997, vol. 36, pp. 399–404.
10. R.C. Atwood and P.D. Lee: *Metall. Mater. Trans. B*, 2002, vol. 33B, pp. 209–21.
11. P.D. Lee, A. Chirazi, and D. See: *J. Light Met.*, 2001, vol. 1, pp. 15–30.
12. D.M. Stefanescu: *Int. J. Cast Met. Res.*, 2005, vol. 18, pp. 129–43.
13. K.D. Carlson and C. Beckermann: *Metall. Mater. Trans. A*, 2009, vol. 40A, pp. 163–75.
14. K.D. Carlson, Z. Lin, and C. Beckermann: *Metall. Mater. Trans. B*, 2007, vol. 38B, pp. 541–55.
15. E. Niyama, T. Uchida, M. Morikawa, and S. Saito: *AFS Int. Cast Met. J.*, 1982, vol. 7, pp. 52–63.
16. J. Guo, C. Beckermann, K.D. Carlson, D. Hirvo, K. Bell, T. Moreland, J. Gu, J. Clews, S. Scott, G. Couturier, and D. Backman: *IOP Conf. Ser.*, 2015, vol. 84, p. 012003.
17. L. Yao, S. Cockcroft, J. Zhu, and C. Reilly: *Metall. Mater. Trans. A*, 2011, vol. 42A, pp. 4137–4148.
18. F.G. Blake: *Acoustic Research Laboratory Harvard University*, 1949, Technical Memoranda No. 12.
19. C.E. Brennen: *Cavitation and Bubble Dynamics*, Cambridge University Press, Cambridge, 2013.
20. D.M. Stefanescu and A.V. Catalina: *Int. J. Cast Met. Res.*, 2011, vol. 24, pp. 144–50.
21. M. Felberbaum, E. Landry-Désy, L. Weber, and M. Rappaz: *Acta Mater.*, 2011, vol. 59, pp. 2302–08.
22. JMatPro, Sente Software Ltd., Surrey Technology Center, Surrey GU2 7YG, United Kingdom.
23. D. Emadi and J.E. Gruzleski: *AFS Trans.*, 1994, vol. 102, pp. 307–12.
24. Q.T. Fang and D.A. Gragner: *AFS Trans.*, 1989, vol. 97, pp. 989–1000.